Fall 2019

Estimating electromagnetic emissions from a site installation with multiple racks of server equipment

Ze Sun

Department:

ESTIMATING ELECTROMAGNETIC EMISSIONS FROM A SITE INSTALLATION WITH MULTIPLE RACKS OF SERVER EQUIPMENT

by

ZE SUN

A THESIS

Presented to the Graduate Faculty of the

MISSOURI UNIVERSITY OF SCIENCE AND TECHNOLOGY

In Partial Fulfillment of the Requirements for the Degree

MASTER OF SCIENCE

in

ELECTRICAL ENGINEERING

2019

Approved by:

Jun Fan, Advisor
Chulsoon Hwang
Daryl Beetner

ABSTRACT

There are hundreds, sometimes even thousands, of servers working simultaneously inside a data center. Their radiation can be a problem and cause EMI issues. However, it is not feasible to perform full-wave simulation of these racks because of the large electric size of the model. In this thesis, an algorithm is proposed to predict the emission form rack array. The equivalent dipole source is extracted from EMI measurement data of a single rack and used as the radiation source in the multiple rack model. The coupling between racks cannot be ignored, but through the simulation, it is also found that only those located near the radiation source will have a significant impact on the final result. In this way, the contribution of each rack to the final electromagnetic field distribution can be calculated using a model with only a few racks included. In order to accelerate the simulation further, racks in the array are divided into several groups. Racks in the same group are located at similar positions in the array, and their contribution can be calculated using one model. After the simulation is done, the emissions from each single rack are added together to get the final prediction result. Each step of the simplification is validated by measurement and simulation, and the final predicted result agrees with the measurement result.

ACKNOWLEDGMENTS

I would like to express my great gratitude to my advisor, Prof. Jun Fan, for his guidance and encouragement throughout my Master's studies. His advice and constant support helped me overcome many difficulties in research. I learned a lot from him about how to work with others, which is very important for my future career. I would also like to thank my committee members, Prof. Chulsoon Hwang and and Prof. Daryl Beetner, for their help and advice on my research work.

I also feel grateful to Yansheng Wang, Nicholas Erickson, Xu Wang, Chunyu Wu and many other senior students in EMC lab. They helped me a lot both in my research work and in my daily life. I spent a happy time studying with them in Rolla.

Last but not least, thanks to the EMC laboratory who supported me during the last two and a half years. I am very lucky and glad to be a graduate student in the lab. Many thanks and best wishes to everyone in the EMC Laboratory!

TABLE OF CONTENTS

Page

LIST OF ILLUSTRATIONS

Figure Page

LIST OF TABLES

Table Page

SECTION

1. INTRODUCTION

With the development of the high-tech industry, data centers housing huge computer systems have been constructed to meet the demand for fast internet connectivity and numerical calculations. Usually, there will be hundreds or even thousands of server racks working simultaneously in a data center. Electromagnetic interference (EMI) caused by power equipment and radio signals can interfere with the nearby antenna severely [1, 2]. Traditionally, sever systems are tested in an EMI chamber or Open Area Testing Site (OTAS) for EMI compliance with a typical configuration [3]. In these measurements, the maximum number of racks under testing is limited by the space of the EMI chamber or OATS. Thus, it is highly desirable to predict the electromagnetic emissions from the entire system based on the available measurement results.

There are two factors that need to be considered when estimating the overall radiation from a site with many racks of server equipment. One is the radiation source, and another is the coupling and scattering between racks. There are many different methods proposed to include these two factors in the simulation.

Since the noise source inside the racks is too complicated to measure [4, 5, 6] and model, the emission pattern of one rack can be measured and replaced with some equivalent sources in the simulation. There are several different methodologies to reconstruct the radiation source. Many works use the current distribution on Huygen's surfaces around the radiation source to quantify the emission from the real source [7, 8, 9]. The equivalent electric current J_s or magnetic current M_s are distributed on the Huygen's box warping up the rack and with the corresponding perfect magnetic conductor (PMC) or perfect electric

conductor (PEC) boundary conditions. The drawback of this method is that it requires obtaining the electric or magnetic field on a closed surface, which can be difficult to measure.

Another commonly used method is replacing the source with dipole moments. This method has been widely applied in the radio frequency interference (RFI) [10, 11, 12, 13, 14, 15, 16] and IC EMC areas [17, 18, 19]. In [16], a physics-based equivalent magnetic dipole source is extracted based on the current distribution and is used to study the near-field coupling between an LCD panel and a smartphone's cellular antenna. The advantage of dipole moments over current on Huygen's box is that it reveals the intrinsic radiation physics of the radiator [20].

In order to accurately represent the original radiation source, many equivalent dipole source reconstruction methods have been proposed. Traditionally, both magnitude and phase information of near field pattern is required for reconstruction [13], but getting phase information is very challenging in the real application. Recently, Ji proposed an iteration algorithm which only needs near field magnitude information on two planner surfaces above the device under test (DUT) to extract dipole source [21]. The phase information will be retrieved by calculating the propagation of waves between two scanning surfaces. This method works well when the size of the DUT is small and rectangular scanning surfaces can capture most of the radiation power from the source. In this thesis, we are going to reconstruct the equivalent dipole source of a server rack. Since the size of the DUT is too large, cylindrical scanning surface around the DUT instead of rectangular scanning surface above the DUT is used. The propagation of wave in cylindrical coordinate is more complicated than in the cartesian coordinate. And due to the limitation of measurement, the scanning surface cannot capture all the radiation hotspots. For example, the antenna used in EMI measurement is too large and cannot move to the heights below 1 m. In this way, some field information is lost and this method will not work anymore.

The second thing need to be considered in data center modeling is the coupling and scattering of the field between racks. The incident wave will generate induced current and charge on the metal structure of server racks. The total radiation field is the sum of the incident field generated by dipole source and the reflected field generated by induced current and charge. In this thesis, Method of Moments (MoM) is used to calculate reflected field [22]. The problem is the size of the matrix in MoM calculation is determined by the electric size of the model. If the whole rack array is modeled without any simplification, the matrix size will be too large to be calculated. So in this thesis, the rack model will be simplified to meet the requirement for both accuracy and time efficiency.

The thesis is organized as below. Section 2 introduces the physics of dipole source radiation and describes the method of equivalent dipole moment source reconstruction using both magnitude and phase information and using magnitude information only. Section 3 studies the coupling between multiple racks. First, the coupling between two nearby racks is investigated, the proposed simplification method is validated by measurement. Next, the scattered field of the whole rack array is calculated as well. In Section 4, a user-friendly tool is developed to estimate the radiation of data center using the theory introduced in previous sections. Section 5 concludes the thesis.

2. EQUIVALENT DIPOLE MOMENT SOURCE EXTRACTION

2.1. RADIATION FROM INFINITESIMAL DIPOLE

When solving electromagnetic interference issues, infinitesimal electric and magnetic dipoles moments are widely used to represent the antenna under test (AUT) [23] or the noise source [16]. Many of the works use a uniformly distributed antenna array to represent the real emission source [24], and it is purely mathematical with no physical meaning. In order to physically reveal the noise source, others use various methods to determine the equivalent dipole source [21][25]. Both methods use the electric field or magnetic field distribution to reconstruct an equivalent dipole source. The theory they use are the same and will be explained below [26].

The electric field radiated by the electric and magnetic dipole moments can be calculated using Eq. (2.1)-(2.3).

$$\begin{aligned} E_x = &\left[q_2 + q_3\frac{(x-x_e)^2}{R^2}\right]P_x + q_3\frac{(x-x_e)(y-y_e)}{R^2}P_y \\ &+ q_3\frac{(x-x_e)(z-z_e)}{R^2}P_z - q_1(z-z_m)M_y + q_1(y-y_m)M_z \end{aligned} \tag{2.1}$$

$$\begin{aligned} E_y = &\, q_3\frac{(y-y_e)(x-x_e)}{R^2}P_x + \left[q_2 + q_3\frac{(y-y_e)^2}{R^2}\right]P_y \\ &+ q_3\frac{(y-y_e)(z-z_e)}{R^2}P_z + q_1(z-z_m)M_x - q_1(x-x_m)M_z \end{aligned} \tag{2.2}$$

$$\begin{aligned} E_z = &\, q_3\frac{(z-z_e)(x-x_e)}{R^2}P_x + q_3\frac{(z-z_e)(y-y_e)}{R^2}P_y \\ &+ \left[q_2 + q_3\frac{(z-z_e)^2}{R^2}\right]P_z - q_1(y-y_m)M_x + q_1(x-x_m)M_y \end{aligned} \tag{2.3}$$

In the equations above, the electric dipole and magnetic dipole are located at (x_e, y_e, z_e) and (x_m, y_m, z_m), respectively. The electric dipole moment in x, y, z directions are P_x, P_y, and P_z, respectively; The magnetic dipole moment in x, y, z directions are M_x, M_y, and M_z, respectively. The electric field strength in x, y, z directions at the location of (x, y, z) are E_x, E_y, and E_z, respectively. And q_1, q_2, and q_3 are three coefficients defined as

$$q_1 = k^2 c_1 G \tag{2.4}$$

$$q_2 = -jk\eta c_2 G \tag{2.5}$$

$$q_3 = -jk\eta c_3 G \tag{2.6}$$

where k is the wave number, η is the wave impedance, G is the free-space Green's function defined as

$$G = \frac{e^{-jkR}}{4\pi R} \tag{2.7}$$

where $R = \sqrt{(x-x')^2 + (y-y')^2 + (z-z')^2}$ is the distance between source point (x, y, z) and observation point (x', y', z'). c_1, c_2, and c_3 are three coefficients defined as $c_1 = \frac{1}{(kR)^2} + \frac{j}{kR}$, $c_2 = 1 - c_1$, and $c_3 = 3c_1 - 1$, respectively.

When multiple dipole sources located at different positions are simultaneously radiating at the same frequency, the total radiation pattern is the linear combination of contribution from each single dipole. Eq. (2.8) is the matrix form equation that calculate the observed E-field at the n-th observation point radiated by the dipole source at the m-th location. $[DM]_m$ shown in Eq. 2.9 is the dipole moments located at the m-th location, each

component corresponds to one electric or magnetic dipole in x, y, or z directions. $[T]_{nm}$ shown in Eq. 2.10 is a three by six matrix containing the transfer function between one dipole source and the radiation field at one observation point.

$$E_n = \begin{bmatrix} E_{x,n} \\ E_{y,n} \\ E_{z,n} \end{bmatrix} = \begin{bmatrix} T_{xnm} \\ T_{ynm} \\ T_{znm} \end{bmatrix} DM_m \tag{2.8}$$

$$DM_m = \begin{bmatrix} P_{x,m} \\ P_{y,m} \\ P_{z,m} \\ M_{x,m} \\ M_{y,m} \\ M_{z,m} \end{bmatrix} \tag{2.9}$$

$$T_{x_{nm}} = \begin{bmatrix} q_2 + q_3 \frac{(x-x')^2}{R^2} \\ q_3 \frac{(x-x')(y-y')}{R^2} \\ q_3 \frac{(x-x')(z-z')}{R^2} \\ 0 \\ -q_1 (z-z') \\ q_1 (y-y') \end{bmatrix}^T, \quad T_{y_{nm}} = \begin{bmatrix} q_3 \frac{(y-y')(x-x')}{R^2} \\ q_2 + q_3 \frac{(y-y')^2}{R^2} \\ q_3 \frac{(y-y')(z-z')}{R'} \\ q_1 (z-z') \\ 0 \\ -q_1 (x-x') \end{bmatrix}^T, \quad T_{z_{nm}} = \begin{bmatrix} q_3 \frac{(z-z')(x-x')}{(z-z')(y-y')} \\ q_2 + q_3 \frac{R^2 (y-y')}{R^2} \\ q_2 + q_3 \frac{(z-z')^2}{R'} \\ -q_1 (y-x') \\ q_1 (x-x') \\ 0 \end{bmatrix}^T \tag{2.10}$$

Finally, the relationship between the E-field at N different observation points and dipole source at M locations can be written as:

$$E = \begin{bmatrix} [E_1]_{3\times1} \\ \vdots \\ [E_n]_{3\times1} \\ \vdots \\ [E_N]_{3\times1} \end{bmatrix} = TX \tag{2.11}$$

where X is the list of dipole sources and T is the transfer function between all the dipole sources and all the observation points.

$$T = \begin{bmatrix} T_{11} & \cdots & T_{1m} & \cdots & T_{1M} \\ \vdots & \ddots & \vdots & \ddots & \vdots \\ T_{n1} & \cdots & T_{nm} & \cdots & T_{nM} \\ \vdots & \ddots & \vdots & \ddots & \vdots \\ T_{N1} & \cdots & T_{Nm} & \cdots & T_{NM} \end{bmatrix} \tag{2.12}$$

$$X = \begin{bmatrix} [DM_1]_{6\times1} \\ \vdots \\ [DM_m]_{6\times1} \\ \vdots \\ [DM_M]_{6\times1} \end{bmatrix} \tag{2.13}$$

2.2. EXTRACT DIPOLE SOURCE FROM ELECTRIC FIELD DATA WITH MAGNITUDE AND PHASE INFORMATION

If the position of M observation points and N dipoles are known, the transfer matrix T can be calculated using Eq. (2.12). Furthermore, if the magnitude and phase information of the E-field at observation points are also available, the equivalent dipole sources can be reconstructed using the least-square method, as shown in Eq.(2.14). The

generated dipole sources X will have the same field distribution as the original E-field E, so in some applications, it can be used to replace the original emission source to simplify the calculation.

$$X = (T^T T)^{-1} T^T E \tag{2.14}$$

In reality, the exact position of the equivalent dipole source is usually unknown. In this situation, in order to extract equivalent dipole sources, some optimization algorithms are used to find the best position that can minimize the difference between the desired E-field and the radiation from the reconstructed dipole source. In this thesis, the genetic algorithm (GA) is chosen to optimize the position and type of equivalent dipole source.

The genetic algorithm is a method for solving both constrained and unconstrained optimization problems that is based on natural selection, the process that drives biological evolution. The genetic algorithm repeatedly modifies a population of individual solutions. At each step, the genetic algorithm selects individuals at random from the current population to be parents and uses them to produce children for the next generation. Over successive generations, the population "evolves" toward an optimal solution, which is defined by the objective function [27].

The workflow of equivalent dipole source extraction using GA is shown in Figure 2.1. First, the position of observation points and the corresponding E-field distribution E^{scan} are loaded into the code. This E-field data must contain both magnitude and phase information. Next, the number of dipole sources under optimization is determined by the user, the default value is one since the time needed for optimization will increase dramatically with the increase of unknowns. GA is then used to optimize the position and type of dipole sources. There are six types of dipoles available (P_x, P_y, P_z, M_x, M_y, and M_z), and they can be located anywhere inside the optimization range set by the user. Once the position and type of dipole moments are set, the transfer matrix T is calculated using Eq. (2.12), and the equivalent dipole moments are extracted using Eq. (2.14).

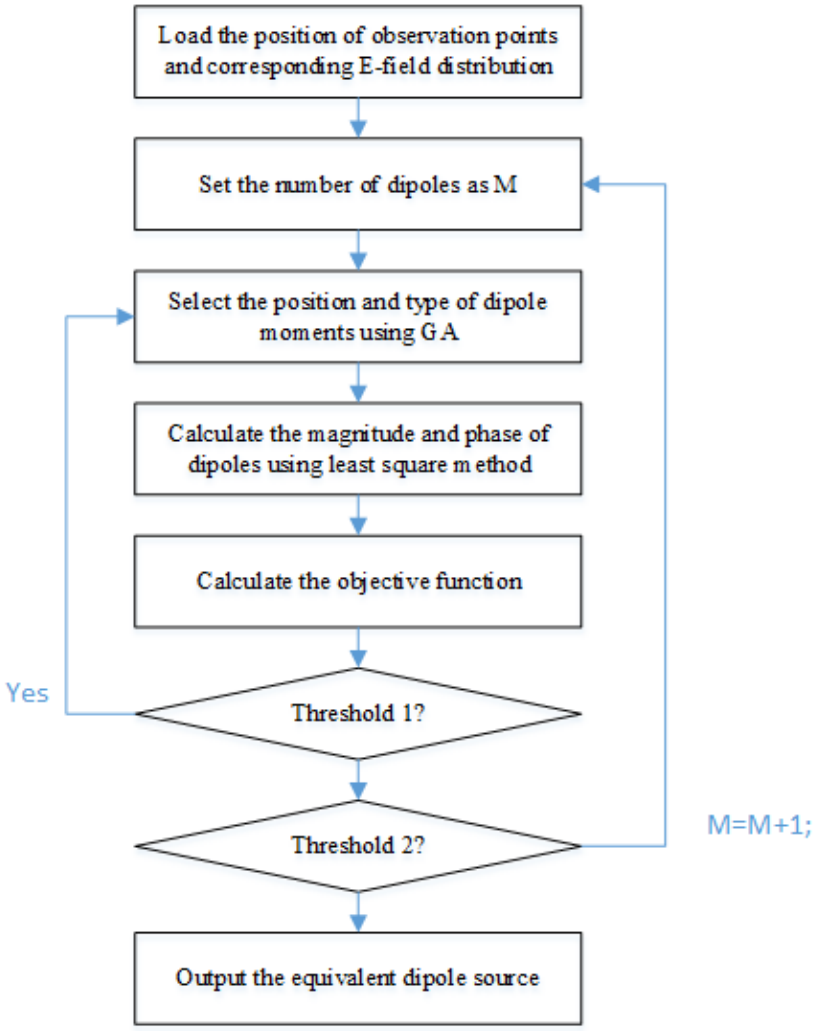

Figure 2.1. Code flow of extracting dipole source using magnitude and phase information of electric field

The radiation pattern of the extracted dipole source E^{fit} may not be the same with the initially loaded E-field distribution E^{scan}. An error function is defined to evaluate the accuracy of the extracted dipole source, which is shown in Eq. (2.15).

$$RE = \sqrt{\frac{\sum[(|E_z^{scan}| - |E_z^{fit}|)^2 + (|E_\varphi^{scan}| - |E_\varphi^{fit}|)^2]}{\sum(|E_z^{scan}|^2 + |E_\varphi^{scan}|^2)}} \tag{2.15}$$

The error function serves as the objective function of GA. If the relative error is larger than the threshold, GA needs to select another set of dipole positions and types in order to reduce the relative error. This process will not end until the minimum relative error is reached or the iteration time exceeds the maximum value.

Sometimes the E-field pattern is too complicated and it cannot be reconstructed using a small number of dipoles. Therefore, after the optimization ends, the value of relative error may still be larger than the limit. If this happens, the number of dipoles will be increased by one, and the optimization process is repeated again. The code can end when the relative error decreases to some threshold value or when the relative error doesn't change too much after adding more dipoles. Then the code will substituent the optimized position and type to Eq. 2.14 to get the final magnitude and phase of dipole moments.

2.3. EXTRACT DIPOLE SOURCE FROM MAGNITUDE-ONLY ELECTRIC FIELD DATA

In the real EMI measurements, the spectrum analyzer is widely used to measure the magnitude of the radiation signal in the frequency domain, and the phase information is usually not available. In this case, the previous method will no longer work. In order to extract equivalent dipole sources, the magnitude information of the electric field on two surfaces are needed. The scanning surface in EMI measurement can be a plane, a cylindrical surface, or a spherical surface. The dipole extraction algorithm discussed below will take E-field data on two cylindrical surfaces as input, but it can be applied to planar scanning and spherical scanning as well.

The cylindrical EMI measurement setup is shown in Figure 2.2. Inside an EMI chamber, the DUT is placed at the center of a rotating table. The receiving antenna is placed at a certain distance away from the DUT. During the measurement, the rotation table will turn to different angles while the antenna is fixed in the same position. In this way, the field on a cylindrical surface around the DUT is measured.

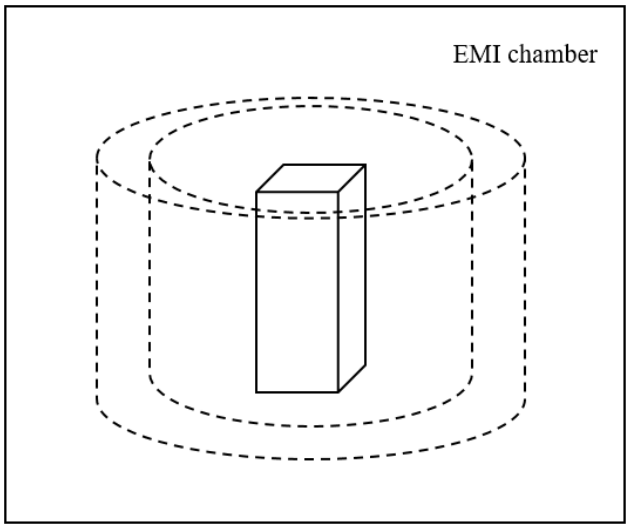

Figure 2.2. Cylindrical EMI measurement setup

The workflow of the proposed equivalent dipole source extraction algorithm is shown in Figure 2.3. The code will first load the magnitude information on two cylindrical surfaces. Next, GA will initialize the position and type of the dipole sources. Then the phase of E-field on every observation point of the outer surface is forced to be zero. Using the loaded magnitude and this initialized phase information, dipole sources can be extracted with the least square method. Then, the code will follow several actions:

Step #1 : Calculate the transfer function between dipole sources and the observation points on the inner surface using Eq. (2.12). Then calculate the field on the inner surface radiated by the current dipole sources.

Step #2 : Calculate the relative error between the calculated result on the inner surface and the loaded field using Eq. (2.15), which is saved as $RE1$.

Step #3 : Since the initial dipole sources are reconstructed from the artificial phase information, the radiation pattern on the inner surface should be different from the loaded field. The code will replace the calculated magnitude result from step one with the loaded information but keep the calculated phase result. This will generate a new set of artificial fields.

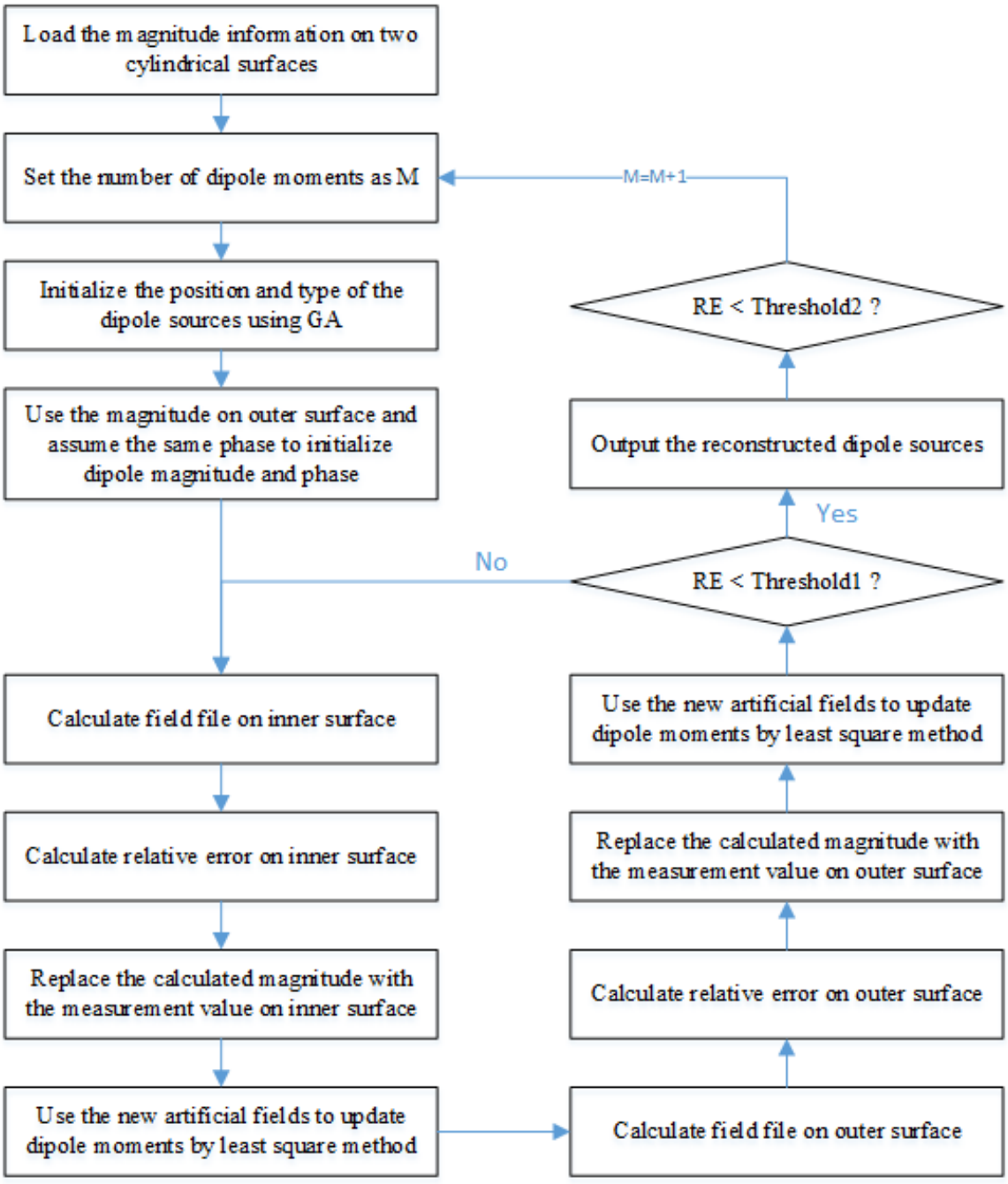

Figure 2.3. Code flow of extracting equivalent dipole source from E-field magnitude information on two scanning surfaces

Step #4 : Use the new artificial fields to update the magnitude and phase of dipole moments by the linear square method.

Step #5 : Calculate the field distribution on the outer surface radiated by the updated dipole source.

Step #6 : Calculate the relative error between the calculated result on the outer surface and the loaded field using Eq. (2.15), which is saved as $RE2$.

Step #7 : Enforce the magnitude of the field on the outer surface to be the loaded data and keep the phase unchanged.

Step #8 : Use the new artificial fields on the outer surface to update the magnitude and phase of dipole moments by the linear square method.

Step #9 : Calculate the average relative error of this iteration $RE = RE1 + RE2$.

As the iteration goes on, the relative error will slowly decrease and converge. After each iteration, the updated RE will be compared with the RE of the previous iteration. If the difference between them is smaller than the criteria, the iteration will stop. Otherwise, the iteration will continue.

The convergence of iteration doesn't mean the equivalent dipole source has been extracted successfully. It only means the calculated magnitude and phase of dipole sources will generate the smallest relative error when the position of these dipoles are fixed at the originally selected positions. When the dipoles are located at other positions, the relative error may be even smaller. Thus, if the average relative error is larger than the threshold, GA will continue to select other positions, and the iteration algorithm will be used again to determine the magnitude and phase of dipole moments. In the end, the code will generate a set of dipole sources that has the smallest relative error compared with the originally loaded field data. If the relative error is still too large, it means the current number of dipoles cannot reconstruct the original field, then the number of dipoles will increase by one and all the steps described above will be repeated again.

2.4. VALIDATION OF THE METHOD WITH INFINITESIMAL DIPOLES AS SOURCE

The proposed method is first validated using the simulation data of two infinitesimal dipoles. The source information is listed in Table 2.1. One Pz dipole is located at (0, 0, 1.5 *m*); its amplitude is 0.5 *Am* and the phase is 0 degrees. Another Px dipole is located at (0.1 *m*, 0, 1.8 *m*); its amplitude is 0.1 *Am* and the phase is 0 degrees. The radius of two cylindrical scanning surfaces are 2 *m* and 5 *m*, respectively. The heights of scanning points are from 1 *m* to 4 *m* with an interval of 0.25 *m*. The azimuthal angle of both surfaces is from 0 degrees to 360 degrees with an interval of 15 degrees.

Table 2.1. Original dipole source and reconstructed equivalent source

Frequency	X (m)	Y (m)	Z (m)	Dipole Type	Amplitude (Am)	Phase (Degree)	RE
Original Model	0 0.1	0 0	1.5 1.8	Pz Px	0.5 0.1	0 0	-
1GHz	0.0037 0.1076	-0.0016 -0.0021	1.4995 1.8052	Pz Px	0.5003 0.1160	-0.0090 0.8847	0.1533
10GHz	6.7e-5 -0.1768	-2.9e-4 0.1803	1.5001 1.7250	Pz Px	0.5015 0.1104	-0.4927 -9.7002	0.1632

The magnitude values of the E-field on two scanning surfaces are imported into the code. GA will optimize the position and type of dipoles. The pre-defined optimization range of the dipole position in the x coordinate is from -0.5 *m* to 0.5 *m*, while in the y coordinate it is from -0.5 *m* to 0.5 *m*, and in the z coordinate it is from 1 *m* to 2 *m*. The optimization range of dipole type is from 1 to 6, which represents the electric dipole and magnetic dipole in x, y, z directions. In the beginning, the number of dipoles under optimization is one. After the relative error converges, since the difference between the original field and the reconstructed field is too large, the number of dipole sources will be increased to two. The final optimization result is shown in Table 2.1. When using the field distribution at 1 GHz as the input, the relative error will converge to 0.1533. The

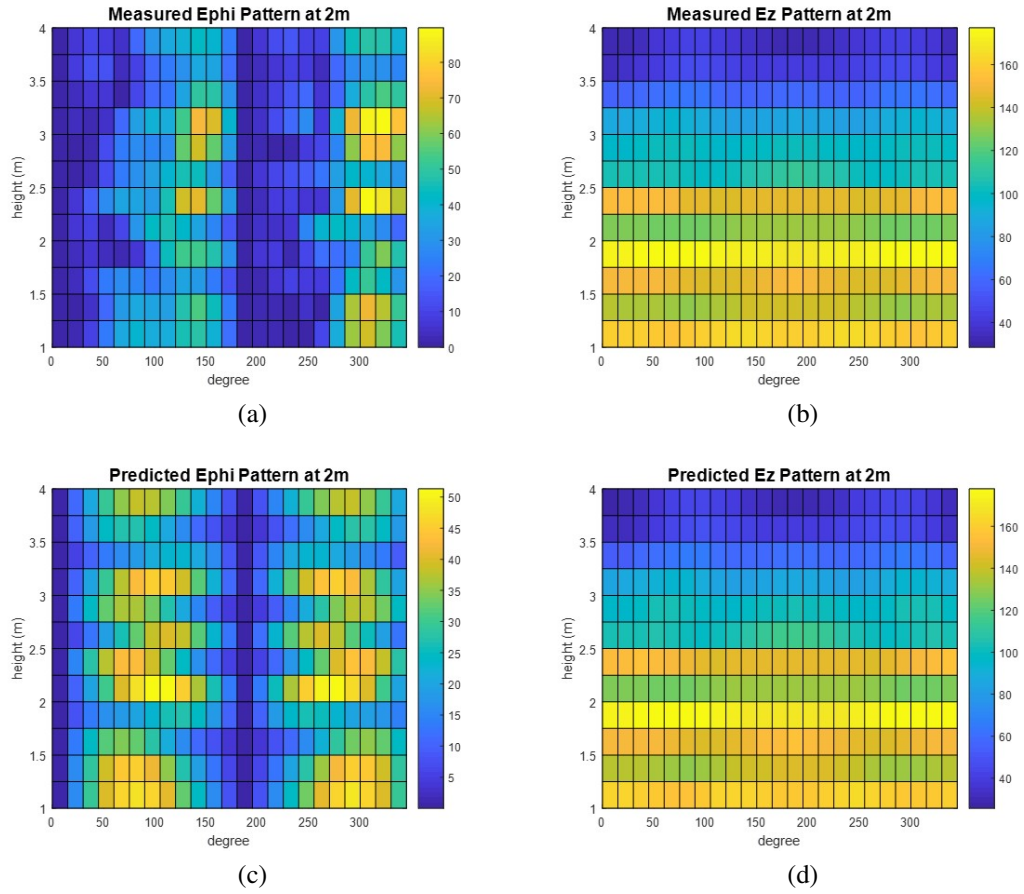

Figure 2.4. 2.4a: Original simulation: Ephi component distribution on the cylindrical surface. 2.4b: Original simulation: Ez component distribution on the cylindrical surface. 2.4c: Reconstructed field: Ephi component distribution on the cylindrical surface. 2.4d: Reconstructed field: Ez component distribution on the cylindrical surface.

reconstructed dipoles have a similar position, magnitude, and phase to the original model. The original and reconstructed field distribution on the inner scanning surface is shown in Figure 2.4. The x-axis is the azimuthal angle in degrees, while the y-axis is the height of observation points. The unit of the data is $dB\mu V/m$. The reconstructed E-field component in the vertical direction (Ez) is nearly the same as the original field, while the horizontal component (Ephi) is a little bit different from the original. This is because the magnitude of Ez is much larger than Ephi, so Ez plays a more important role in the equivalent source extraction. Using the field at 10 GHz, the equivalent source can also be reconstructed with a relative error of 0.1632, as shown in Table 2.1.

2.5. VALIDATION OF THE METHOD WITH RADIATING RACK AS SOURCE

This thesis aims to estimate the radiation from multiple racks in the data center. Here, the radiation from one server rack is measured, and the equivalent dipole source is reconstructed. Since the generation mechanism of EMI radiation and the structure of noise source is not studied here, replacing with dipole moments will accelerate the calculation without affecting the accuracy.

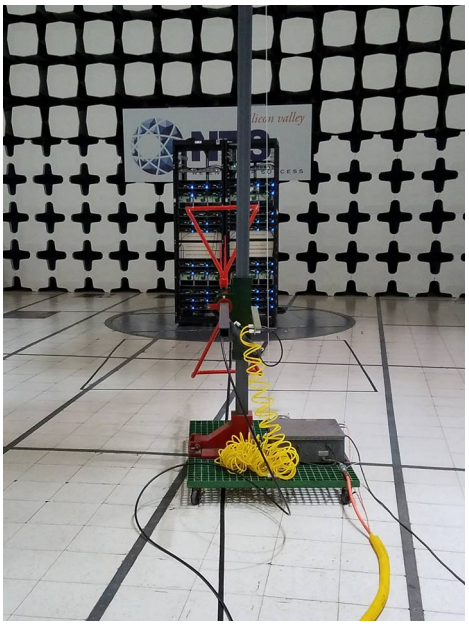

Figure 2.5. Measurement Setup of the EMI measurement

The measurement setup is shown in Figure 2.5. The racks will radiate at 781.25 MHz. The radius of the cylindrical scanning surfaces are 2 m and 5 m, respectively. The scanning height is from 1 m to 4 m, and the distance between two successive observation points is 0.25 m in z direction. The rotation table will turn from 0 degrees to 360 degrees and stop every 15 degrees.

The measured E-fields are shown in Figure 2.6. It is found that the rack will mainly radiate from the front side, and there is little emission from the other sides. It is because only the front side is left open, and all the other sides are shielded with metal structure. This feature can be used to simplify our multiple rack simulation later.

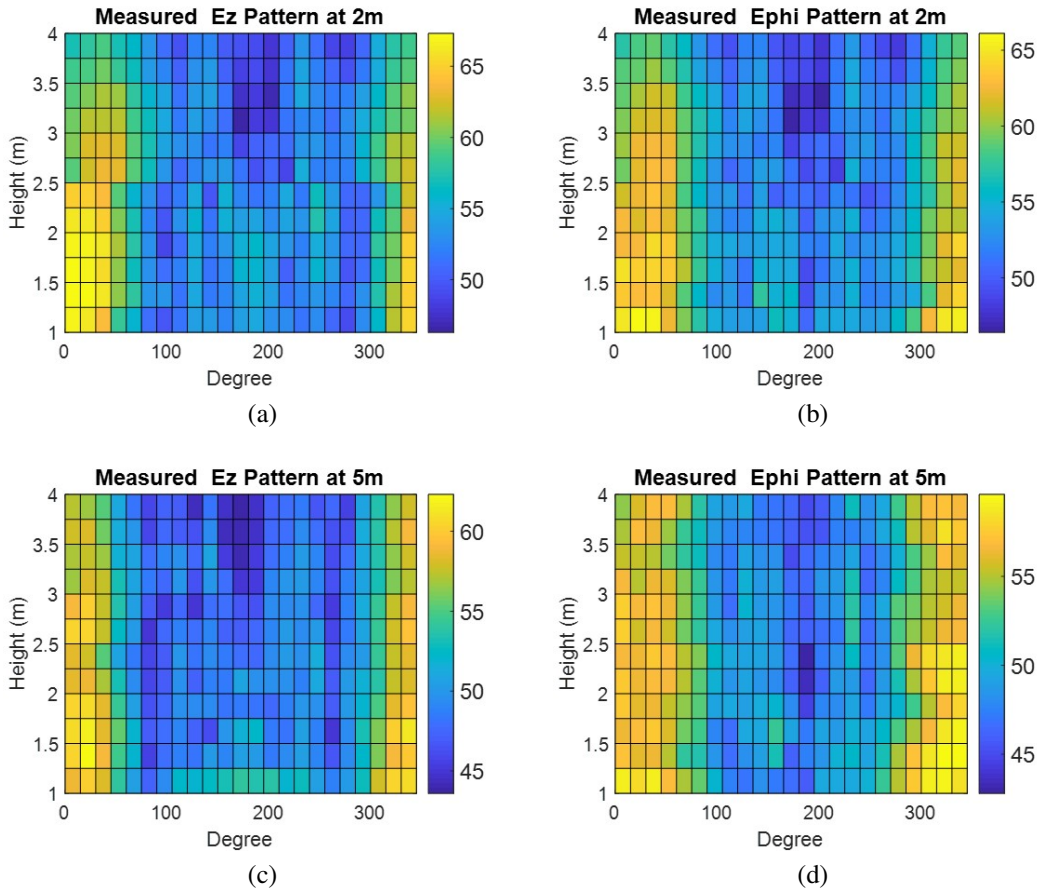

Figure 2.6. 2.6a: Measured Ez component distribution on the inner scanning surface. 2.6b: Measured Ephi component distribution on the inner scanning surface. 2.6c: Measured Ez component distribution on the outer scanning surface. 2.6d: Measured Ephi component distribution on the outer scanning surface.

The measurement data is loaded into the dipole reconstruction code discussed in section 2.3. The output of the algorithm are nine dipole moments with a relative error of 0.1885. Radiation pattern of the equivalent dipole source on two scanning surfaces are shown in Figure 2.7. The reconstructed fields match well with the measurement results, and they have similar maximum values and hotspot positions.

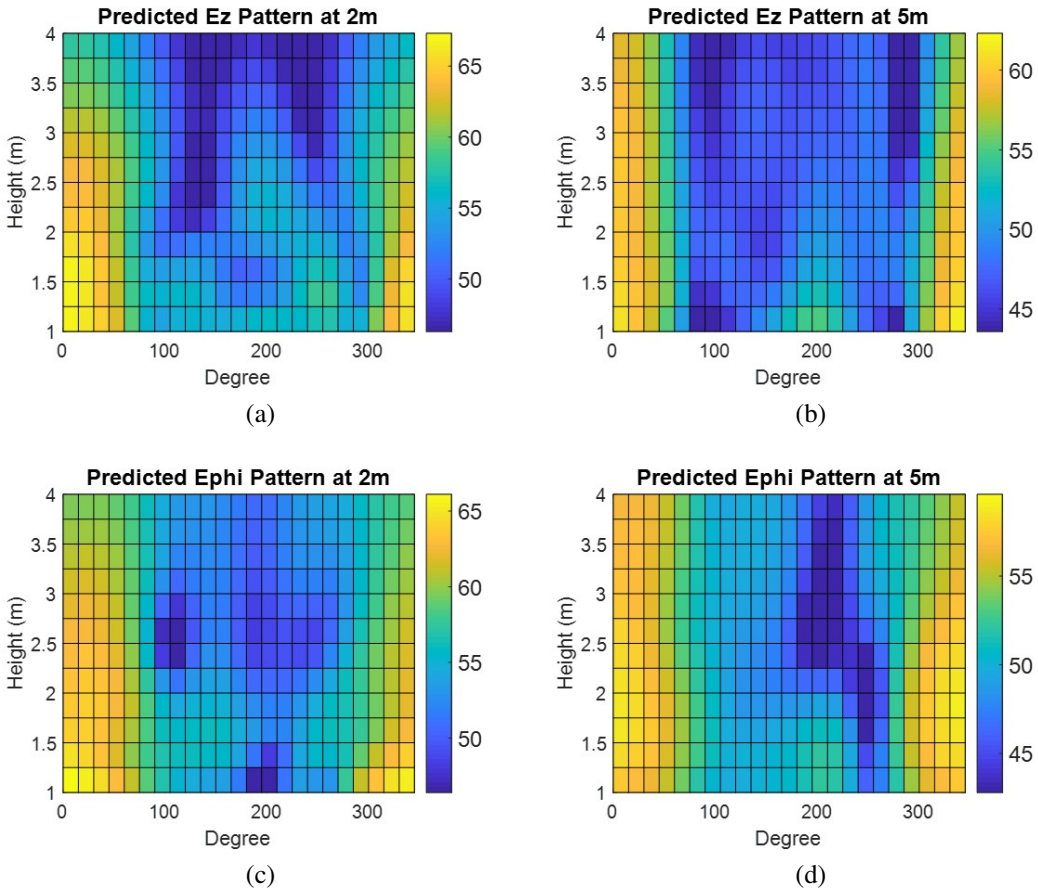

Figure 2.7. 2.7a: Reconstructed Ez component distribution on the inner scanning surface. 2.7b: Reconstructed Ephi component distribution on the inner scanning surface. 2.7c: Reconstructed Ez component distribution on the outer scanning surface. 2.7d: Reconstructed Ephi component distribution on the outer scanning surface.

3. MULTIPLE RACKS RADIATION MODELING

3.1. RADIATION FROM RACKS IN DATA CENTER

In the real data center, there can be hundreds or even thousands of server racks working simultaneously. The servers, network equipment, and cables may generate and emit a strong electromagnetic frequencies, and their performance may also be affected by the external radiations as well. However, it is not practical to build a full-wave model of all the racks and simulate the radiation from them because it is too time-consuming and requires a large amount of computation source. It is also wrong to simulate the radiation from every single rack separately and then add them up together because strong coupling occurs among racks due to reflection and scattering.

In this section, an algorithm is proposed to accurately estimate the total radiation from the data center. In section 2, the radiation pattern on a cylindrical surface from one rack is measured using the typical EMI testing setup, and the equivalent radiation sources are then extracted from measurements. It is used as the excitation source in the future simulation. The rack-to-rack coupling is modeled using full-wave EM simulations with reasonable simplification. The measurement and simulation results show that when one rack is working, the radiation field will be scattered by the racks nearby, while the racks that are far away from it will have little effect on the final emission pattern. Thus, only the nearby racks need to be included in the full-wave simulation, which will save a significant amount of calculation time. After the radiation from each rack is known, the total EM field distribution from a site can then be efficiently calculated by vector summing the contributions of all the equivalent sources.

3.2. COUPLING BETWEEN TWO RACKS

Scattering between the metal structures of racks can significantly change the field distribution. However, it is not feasible to measure the coupling between a bunch of racks in an EMI chamber because of the limited size of the turntable. In order to model this effect and perform the measurement to validate the simulation result, the scattering between two racks is studied first. In the data center, two nearby racks can be placed face-to-face, back-to-back, and side-by-side with each other. From the measurement result in the previous section, the radiation from a rack is mainly in the front direction, and there is little emission from the left, right, back, and top sides of the rack. Therefore, it is reasonable to assume that the relative position and direction of two racks will affect the scattering between them. And the three placement arrangements will be studied one-by-one as follows.

3.2.1. Two Racks Back to Back. Since there is little electromagnetic field radiating from the backside of the rack, when the two racks are placed back-to-back, the scattering between them does not need to be included in the modeling. This statement is first validated by the simulation.

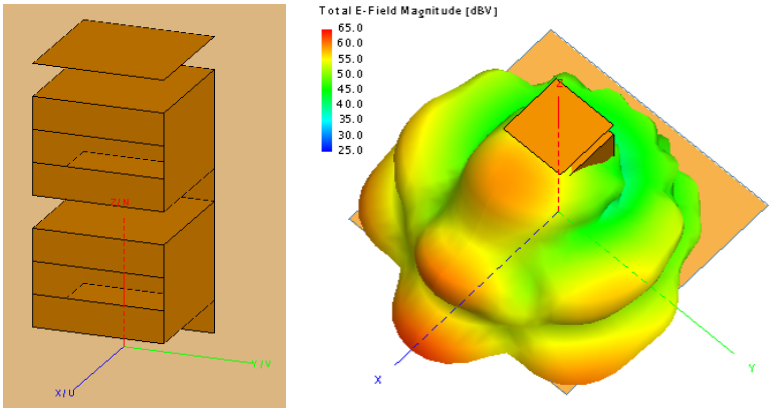

(a) (b)

Figure 3.1. 3.1a: Simulation rack structure. 3.1b: Far-field radiation distribution of the rack model.

A rack structure is built in the full-wave solver FEKO [28]. The width, length and height of the rack is 0.8 m, 0.8 m, and 1.8 m, respectively. There are two openings in the front panel, and the other sides are covered with metal sheet. This model will radiation at 600 MHz mainly in the front direction, as shown in Figure 3.1. When the two racks are placed back-to-back and radiate simultaneously, the far-field distribution is shown in Figure 3.2.

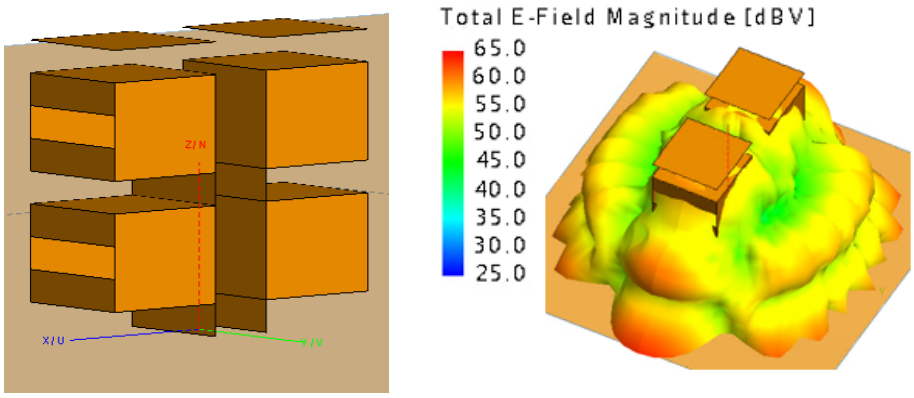

(a) (b)

Figure 3.2. 3.2a: Two rack models are place back to back in simulation. 3.2b: Far-field radiation distribution when two racks are radiating simultaneously.

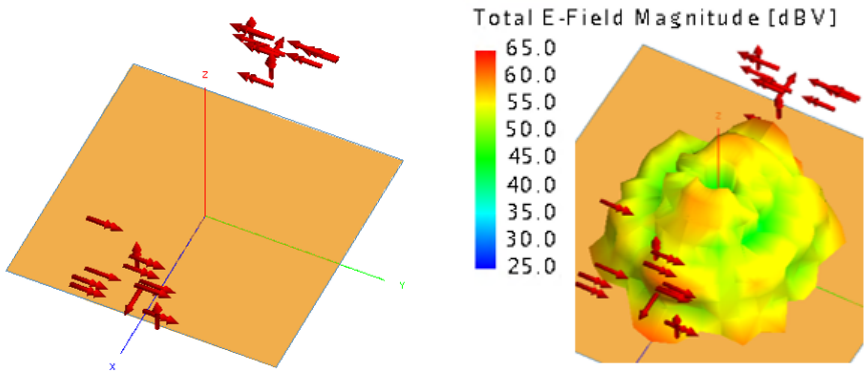

(a) (b)

Figure 3.3. 3.3a: Put two sets of dipole moments back to back with each other. 3.3b: Far-field radiation distribution.

Next, the equivalent dipole source is reconstructed using the previously discussed algorithm. Then, two sets of dipole sources are put in the same position as the two racks in Figure 3.2a. One set of dipoles radiates at +x direction, while the other is turned 180 degrees and radiates at -x direction. Since there is no metal structure in the model, the scattering between two racks is neglected. The resulting far-field distribution in Figure 3.3 is very similar to the one in Figure 3.2, which means the impact of scattering can be excluded when two racks are placed back-to-back with each other.

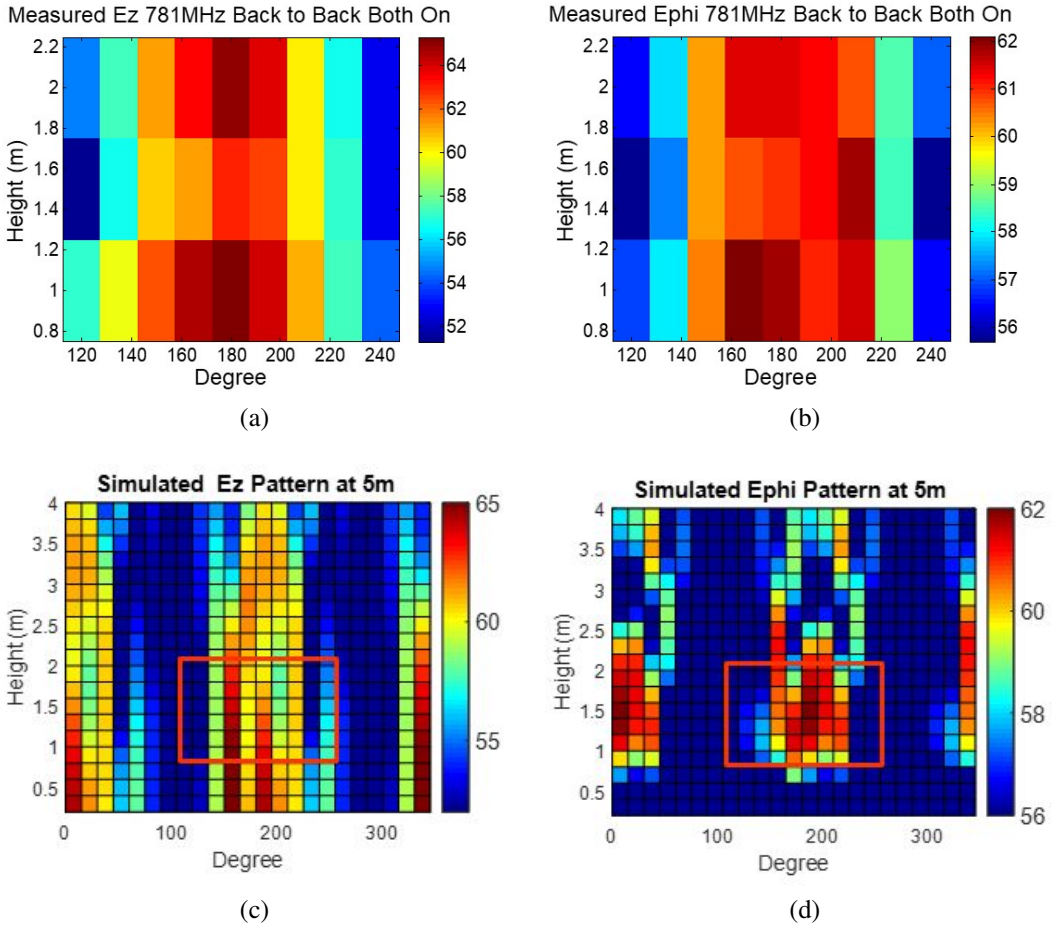

Figure 3.4. 3.4a: Measured Ez component distribution on the cylindrical surface when two racks are placed back to back. 3.4b: Measured Ephi component distribution on the cylindrical surface. 3.4c: Simulated Ez component distribution on the cylindrical surface. 3.4d: Simulated Ephi component distribution on the cylindrical surface.

This theory can be further validated by real measurement. Two racks under test are placed back-to-back with each other and radiate simultaneously at 781 MHz. The distance between the two racks is 1 m. Since the two racks are equipped with the same type of servers and have the same structure, their emissions are assumed to be the same. So when they are placed back to back, the field distribution should be symmetric. In order to minimize the measurement time, only a portion of the cylindrical scan surface is measured. The field distribution is shown in Figure 3.4. Next, we use two sets of equivalent sources to predict the field distribution. The measurement and simulation results agree with each other, which validates the hypothesis.

3.2.2. Two Racks Side by Side. Since the radiation at the left and right side is also weak, it is reasonable to guess that when two racks are placed side-by-side, their coupling will not have a significant impact on the total emission. Following the same procedure in section 3.2.1, the far-field pattern of two rack structures and two sets of equivalent dipole sources are compared in Figure 3.5 and Figure 3.6. The similar patterns validate the initial guess.

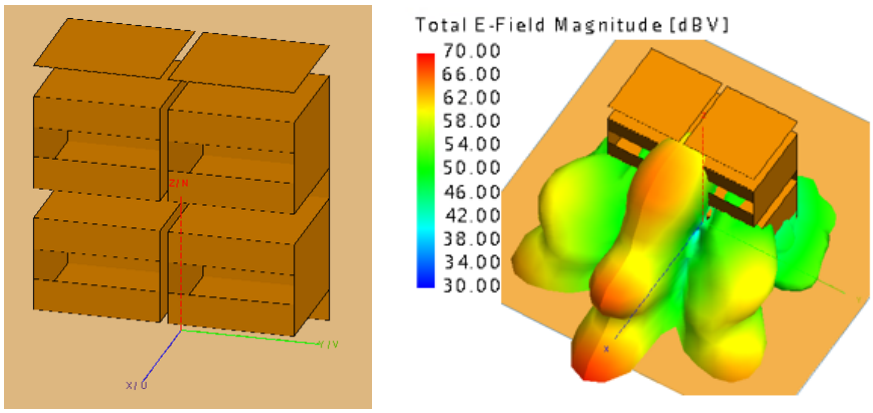

(a) (b)

Figure 3.5. 3.5a: Simulation rack structure. The width, length and height of the rack is 0.8 m, 0.8 m, and 1.8 m, respectively. 3.5b: Far-field radiation distribution when two racks are radiating simultaneously.

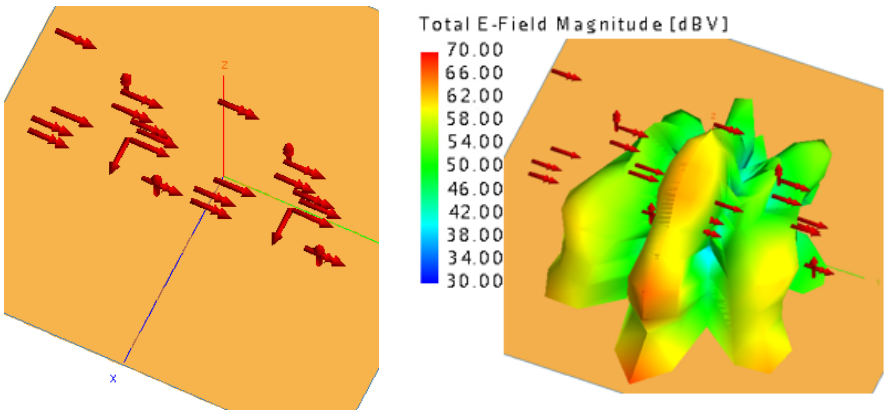

(a) (b)

Figure 3.6. 3.6a: Put two sets of dipole moments side by side. 3.6b: Far-field radiation distribution.

The neglection of coupling in the side-by-side case is further validated by the measurement result shown in Figure 3.7. Two racks radiating at 1.718 GHz are placed side-by-side, the distance between them is 10 cm. Figure 3.7a and 3.7b are the measurement results. The scanning area corresponds to the region in the red box in Figure 3.7c and 3.7d. The pattern distribution is similar between measurement and simulation. The maximum value of the measured Ez component is 59.8 $dB\mu V/m$, while the maximum of the simulated result is 58.8 $dB\mu V/m$. The maximum value of measured Ephi component is 56.0 $dB\mu V/m$, while the maximum of the simulated result is 58.5 $dB\mu V/m$. The variation between the measurement and simulation is within 3 dB for both field components.

3.2.3. Two Racks Face to Face. Since radiation from the front side is very large, there will be strong coupling between two racks when they are placed face-to-face. When one rack is radiating, the induced current will be generated on the surface of another rack. The induced current will significantly change the final field distribution. In this case, the scattering can no longer be neglected, but the simulation model can still be simplified slightly.

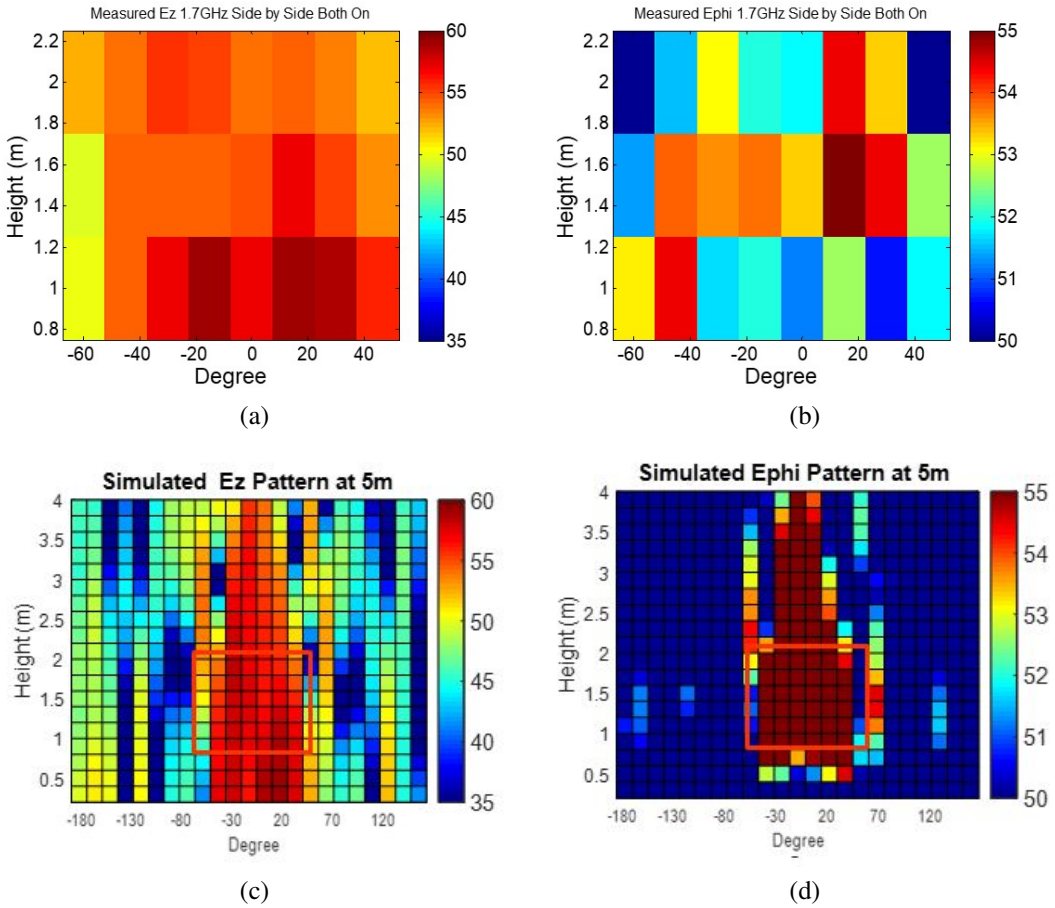

Figure 3.7. 3.7a: Measured Ez component distribution on the cylindrical surface. 3.7b: Measured Ephi component distribution on the cylindrical surface. 3.7c: Simulated Ez component distribution on the cylindrical surface. 3.7d: Simulated Ephi component distribution on the cylindrical surface.

When one rack is radiating, the second rack can be simplified into a metal sheet that is placed at the position of the front panel. This is because the induced current is mainly distributed at the front panel of the second rack. The field generated by the induced current will also propagate back to the radiating rack, which is referred as multiple reflection. In order to include this effect, another metal sheet is needed to block the reflected file. The final simplified model, when only one rack is radiating, is shown in Figure 3.8. The equivalent dipole source is radiating toward the -x direction. One metal sheet is placed at the position of reflector racks's front panel, another is placed at the position of radiator racks's back panel.

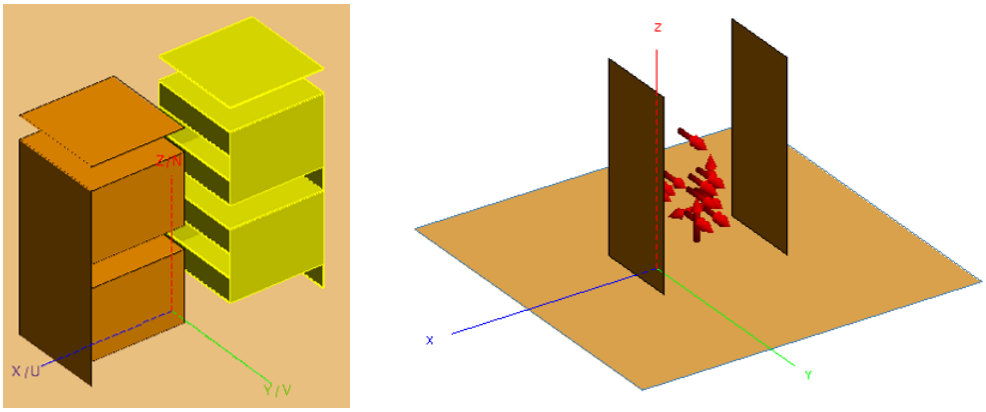

(a) (b)

Figure 3.8. 3.8a: Two racks placed face to face. 3.8b: Simplified model when one rack is radiating.

Adding the field from two simplified models together, we can determine the field distribution when two racks are turned on at the same time. The comparison of simulation results from before and after simplification is shown in Figure 3.9, and the results agree with each other.

The proposed method is also validated by measurement, the results are shown in Figure 3.10. The value of maximum value and the position of hot spot agree well between measurement and simulation.

3.3. SIMPLIFICATION OF RACK ARRAY

In the real application, the placement of racks is more complicated. An example of rack distribution in the data center is shown in Figure 3.11. Each rectangular box represents a server rack, and the missing side of each box indicates the front panel, which is also the main radiation direction of the rack. The orientation of two neighboring rows is different. All the racks are assumed to be the same, which means they share the same structure and equivalent dipole source. Based on the observations in Section 3.2, when simulating radiation from a rack array, even though the multiple scattering cannot be ignored, we can still do some simplification to speed up the calculation.

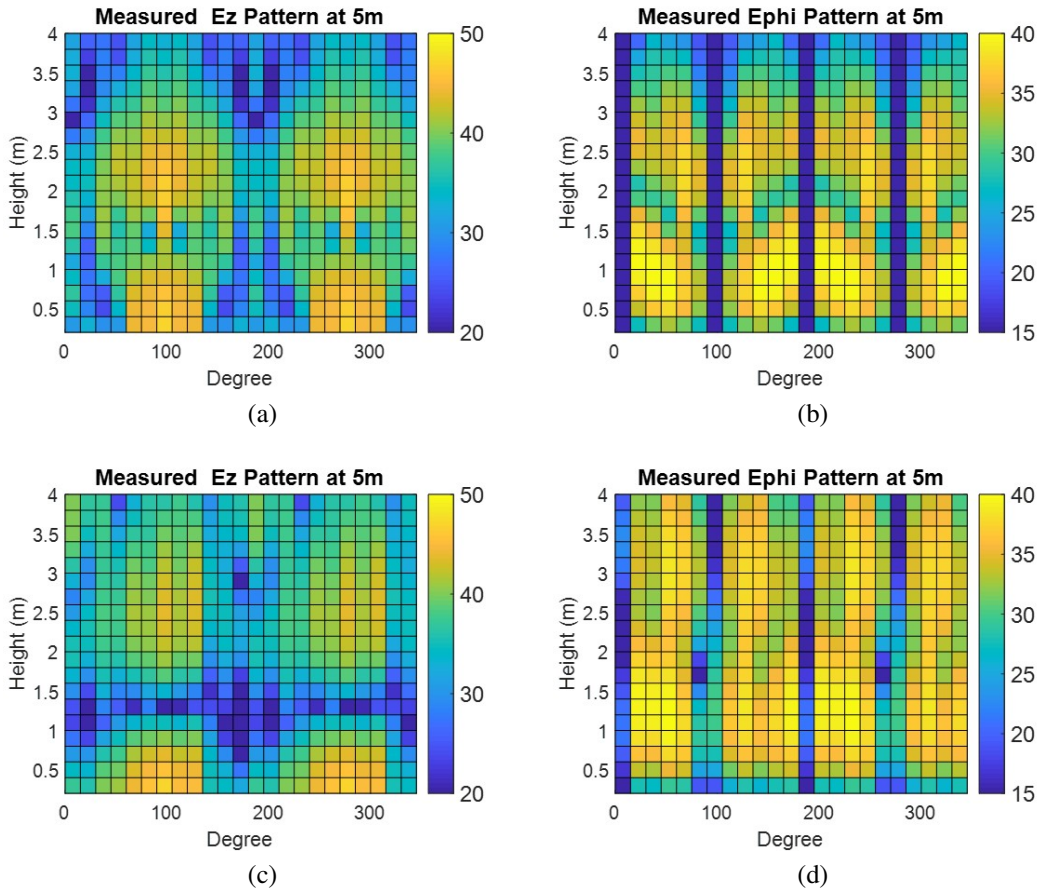

Figure 3.9. 3.9a:Full rack stricture: Ez component distribution on cylindrical surface. 3.9b: Full rack stricture: Ephi component distribution on cylindrical surface. 3.9c: Simplified stricture: Ez component distribution on cylindrical surface. 3.9d: Simplified stricture: Ephi component distribution on cylindrical surface.

3.3.1. Divide the Array into Different Groups. Racks located at different places inside the array will have different contribution to the final radiation pattern. And it is reasonable to guess that if two racks have similar position, their emission should also be similar. Based on this hypothesis, racks in the array are divided into three groups: outer racks, inner racks, and boundary racks. Each group will be treated separately.

Outer racks are those facing out of the array. They can be racks at the first or last row of the array, as shown in Figure 3.11. For an outer rack, the rest of the racks in the array are either back to it or next to it. According to the simulation result in Section 3.2, there is no significant scattering when the outer rack is radiating.

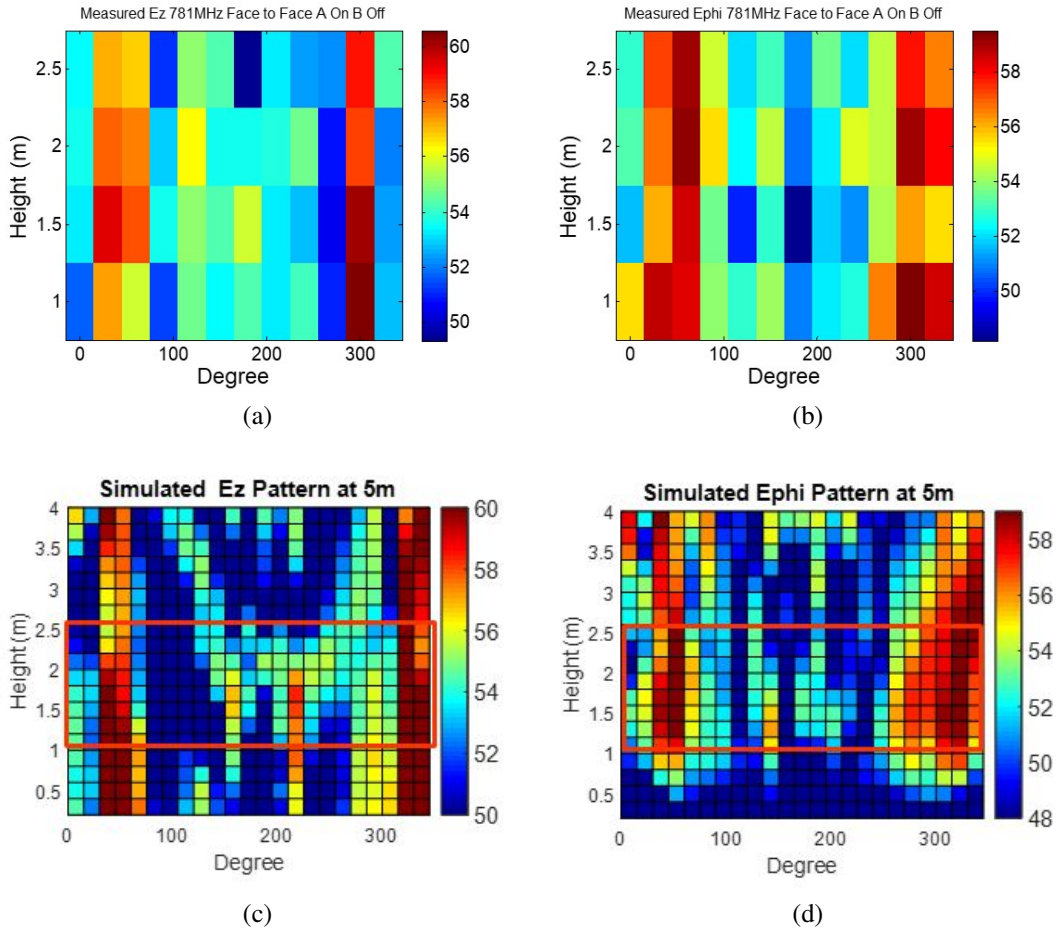

Figure 3.10. 3.10a: Measured Ez component distribution on the cylindrical surface. 3.10b: Measured Ephi component distribution on the cylindrical surface. 3.10c: Simulated Ez component distribution on the cylindrical surface. 3.10d: Simulated Ephi component distribution on the cylindrical surface.

Inner racks are those at the center of the array. They are far away from the array boundary. For each inner rack, it is assumed that there are an infinite number of racks next to it. Besides, boundary racks are those near the array boundary. The criteria to recognize a rack as an inner rack or a boundary rack is related to the radiation frequency, which will be discussed below.

The radiation field will gradually change as it propagates over some distance and scatters for multiple times. For an inner rack, since there are an infinite number of racks next to it, adding more racks next to it will not change the radiation pattern significantly.

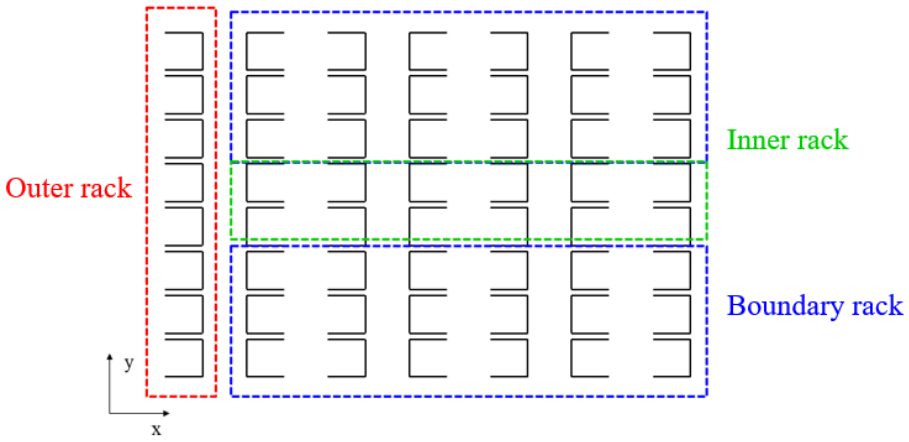

Figure 3.11. Divide the racks in an array into three groups.

This phenomenon can be used to determine whether a rack is an inner rack or not. The simulation model is illustrated in Figure 3.12. A set of equivalent dipole sources is placed at the center of the array. Since only the racks opposite to the source will change the field distribution, only two rows of racks are simulated. The number of racks placed next to it will gradually increase. According to our assumption, when the number of side racks is large enough, the field will finally converge to a certain distribution, and adding more side racks will not change the field distribution much. At this point, the radiation source can be regarded as an inner rack.

Figure 3.13 shows the simulation result when the rack is radiating at 600 MHz. The observation points are located on a circle centered at the radiating rack. The x-axis is the azimuthal angle in degrees. The height of these points are fixed at 5 m. It is clearly shown that when the number of the nearby rack increases from one to two, the peak position changes greatly. However, when the number increases from three to four, the field distributions are almost the same. Consequently, at this frequency, for any rack in an array, if there are three racks on the left of it and three racks on the right of it, adding more side racks will not change its emission field too much, and it can be regarded as an inner rack.

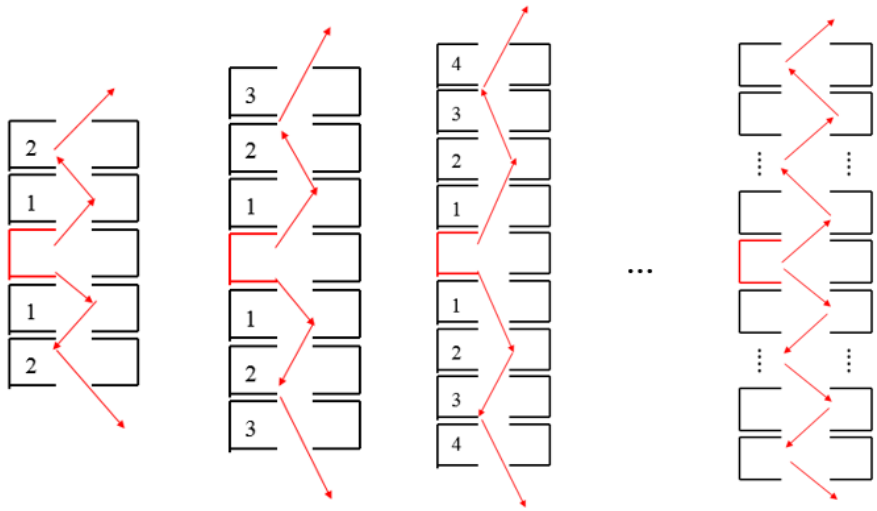

Figure 3.12. Simulation model to determine the definition of inner racks

Table 3.1. Definition of inner rack at different frequencies

Frequency	Wavelength(m)	Length of Nearby Rack (m)	Ratio between Length of Nearby Rack and Wavelength
400MHz	0.75	3.4	4.5
600MHz	0.5	2.55	5.1
900MHz	0.33	1.7	5.15
1.7GHz	0.17	0.85	5

Similar simulations are performed at several different frequencies. The results are shown in Table 3.1. For example, at 400 MHz, the corresponding wavelength is 0.75 m. An inner rack should have at least four racks to the left and right of it, respectively. In the simulation model, the total length of these four racks is 3.4 m, and the ratio between the total length of four racks and the wavelength is 4.5. It is interesting to notice that at different frequencies, these ratios are all around 5. Therefore, this ratio can be used as a rule to determine whether or not a rack is an inner rack at different frequencies. For a particular rack structure radiating at a fixed frequency, multiply the wavelength with five and then divide it by the width of rack, the number of needed nearby rack to define a rack as an inner rack is known.

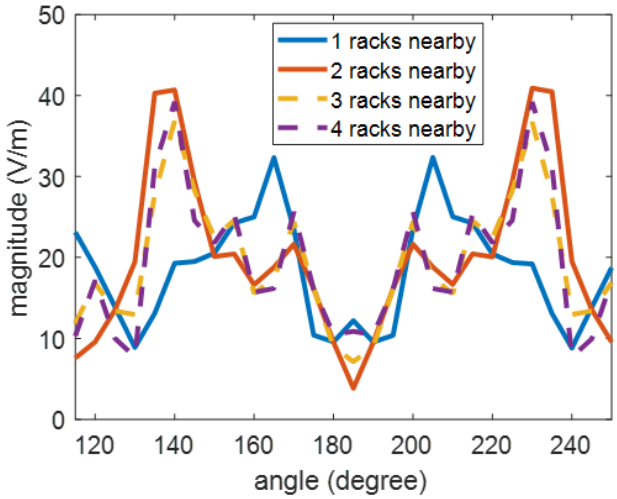

Figure 3.13. Change of field distribution when the number of side rack changes.

3.3.2. Simulation of Racks from Different Groups. After the racks are divided into three groups, they are simulated separately using different simplification strategies. For outer racks, as stated previously, the radiation is not greatly affected by the rest of the racks in the array. Therefore, the field distribution can be calculated by setting the equivalent dipole source on the corresponding rack position. The simulation result shown in Figure 3.14 validates this method. It shows the radiation pattern of one outer rack in Figure 3.11. The simulation frequency is 781MHz. In the original model, there are several rack structures placed next to and back to the radiating rack, the results are shown in Figure 3.14a and 3.14b. After replacing the radiating rack with equivalent dipole sources and deleting the metal structure of all the other racks, the field distribution shown in Figure 3.14c and 3.14d is nearly the same as the original model. Since there are only dipole sources and no other structure in the simplified model, the calculation is very fast.

It is more complicated to simulate inner racks because the scattering and coupling cannot be ignored. However, as stated previously, only the nearby racks have a significant impact on the simulation result. For example, at 781MHz, if there are three racks on the left and right side of the radiating rack, respectively, then this rack can be regarded as

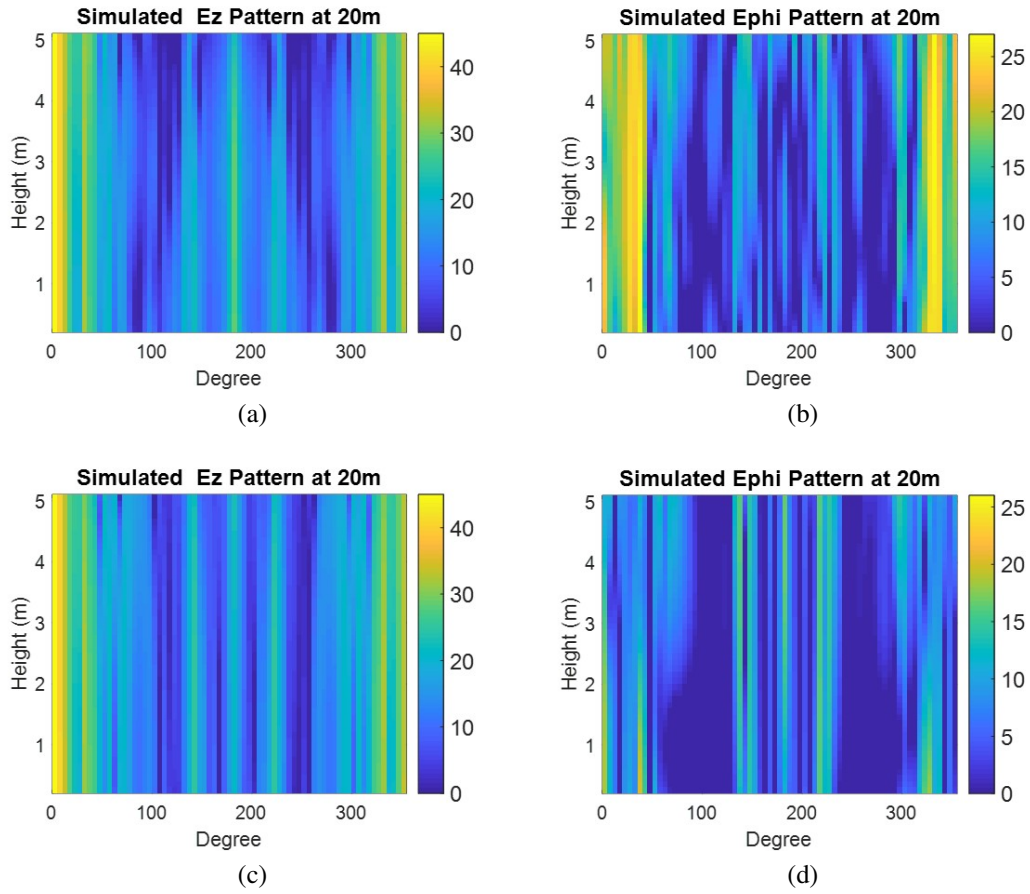

Figure 3.14. 3.14a: Original outer rack simulation: Ez component distribution on the cylindrical surface. 3.14b: Original outer rack simulation: Ephi component distribution on the cylindrical surface. 3.14c: Simplified outer rack simulation: Ez component distribution on the cylindrical surface. 3.14d: Simplified outer rack simulation: Ephi component distribution on the cylindrical surface.

an inner rack, and its emission pattern is dominated by the six racks next to it and the seven racks opposite it. Adding more racks in the model will not change the result too much. Thus, the number of racks under simulation can be greatly reduced. Besides, among the nearby racks surrounding the radiation source, it is found that some plates will be illuminated and induced current will be generated there, while some are shadowed and do not have a significant impact on the scattered field, as shown in Figure 3.15. Therefore, these shadowed faces can be ignored in the simulation as well. In the end, the simplified model of the inner rack at 781MHz is shown in Figure 3.16. There is one radiating rack

and thirteen surrounding racks in this model. The radiating rack is replaced with equivalent dipole source, and a metal sheet is added at the position of its back panel in order to take care of multi-reflection. The five racks right next to the radiation source cannot be simplified greatly, because the induced current generated on their surface is large. However, the racks that are relatively far away from the source can be greatly simplified without introducing too much error. The comparison of field distribution before and after simplification is shown in Figure 3.17.

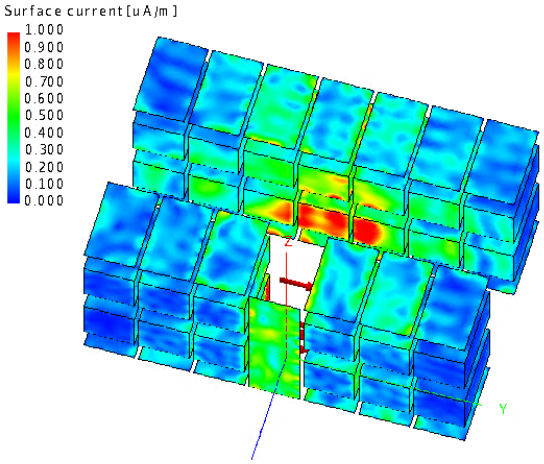

Figure 3.15. Distribution of induced current.

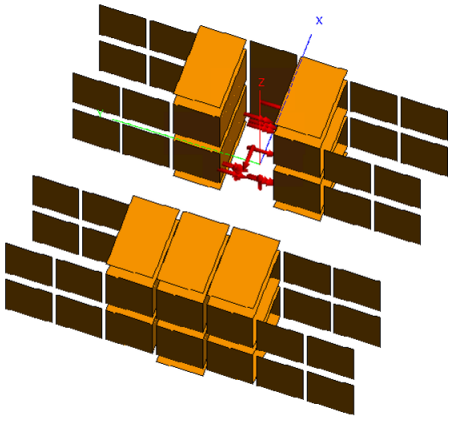

Figure 3.16. Simplified simulation model of inner rack at 781MHz.

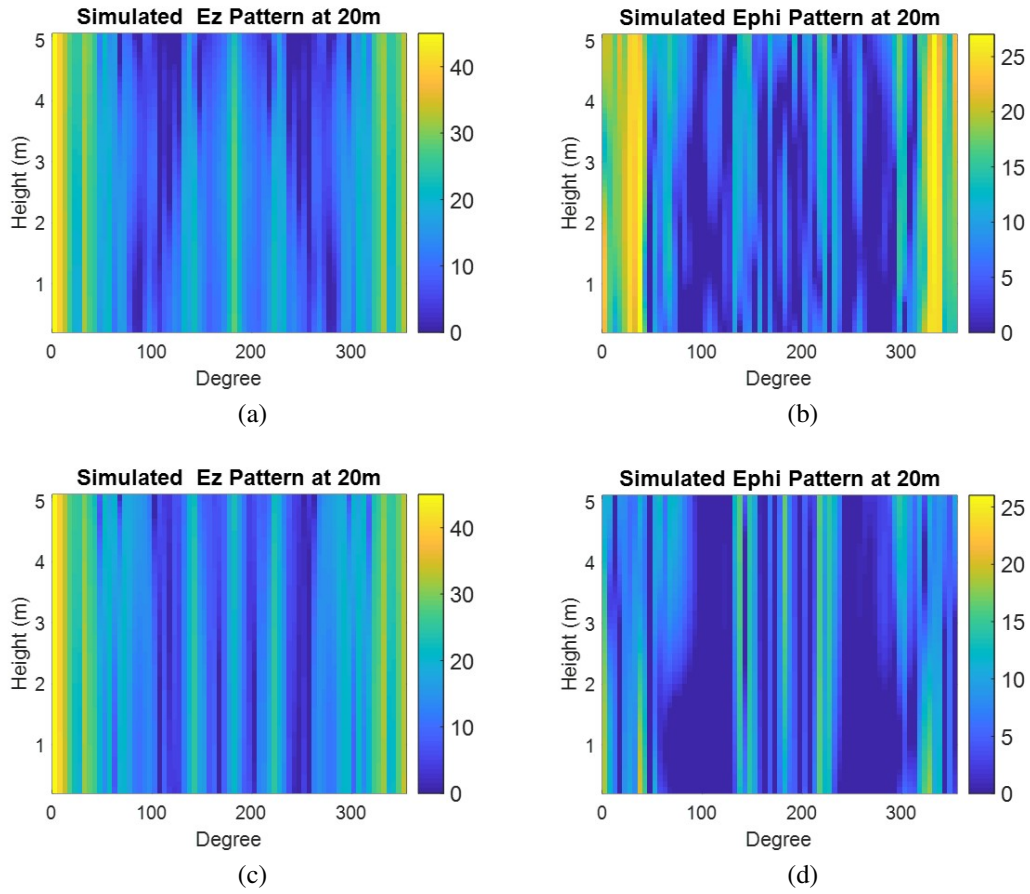

Figure 3.17. 3.17a: Original outer rack simulation: Ez component distribution on the cylindrical surface. 3.17b: Original outer rack simulation: Ephi component distribution on the cylindrical surface. 3.17c: Simplified outer rack simulation: Ez component distribution on the cylindrical surface. 3.17d: Simplified outer rack simulation: Ephi component distribution on the cylindrical surface.

When the rack is radiating at different frequencies, the procedure of simplification is the same. First, the number of racks that need to be included in the model is determined by the simulation frequency. Then the radiating rack is replaced with a metal sheet on the back and equivalent dipole sources. The five racks surrounding the source cannot be simplified too much; only a few panels of them are deleted. Finally, only the front and back panels of the rest racks are kept in the model, all the other panels are neglected.

The simplification process for the outer racks is very similar to inner racks. The only difference is that the nearby racks are not symmetric any more. The simplified model of one boundary rack is shown in Figure 3.18.

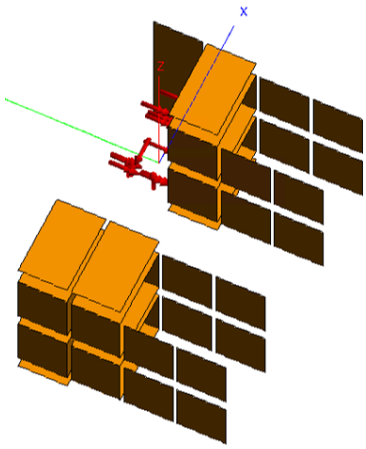

Figure 3.18. Simplified simulation model of inner rack at 781MHz.

As seen in Figure 3.11, there are many inner racks in the array, and all of them can be simplified into the same model shown in Figure 3.16. Traditionally, in order to get the emission from each rack, we need to shift the rack model to different positions while the observation points are fixed. However, we can also fix the position of model and set multiple scanning surfaces. In this way, by performing the simulation for one time, we can determine the radiating field for all inner racks. The same thing happens to boundary racks as well.

After the radiation from every rack are known, they can be summed up together to get emission from the whole array. Figure 3.19 shows the field distribution of a three-by-seven array that is calculated by the original model and the simplified model. The racks on the first row are facing out of the array, so they are outer racks according to our definition. The second row and third row are face-to-face with each other. The results from the two methods agree well with each other, which validates our proposed method.

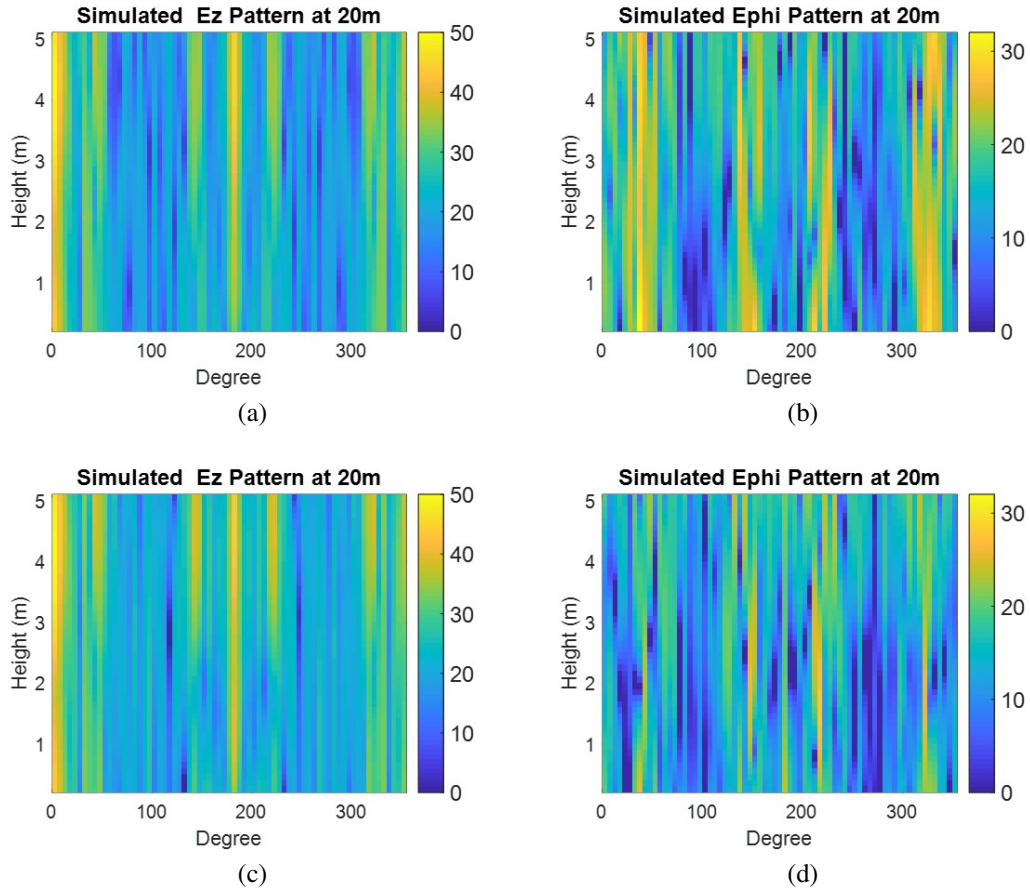

Figure 3.19. 3.19a: Original array simulation: Ez component distribution on the cylindrical surface. 3.19b: Original array simulation: Ephi component distribution on the cylindrical surface. 3.19c: Simplified array simulation: Ez component distribution on the cylindrical surface. 3.19d: Simplified array simulation: Ephi component distribution on the cylindrical surface.

4. TOOL DEVELOPMENT AND VALIDATION

4.1. INTRODUCTION OF TOOL DEVELOPMENT

A software tool is developed for the application related to EMI issues in the data center. There are two main functions in this tool. First, it can use EMI measurement or simulation data on cylindrical surfaces to reconstruct equivalent dipole source. Second, given the array information and source data, it can calculate radiation from multiple racks in the data center.

In order to make the tool user friendly, a Graphical User Interface (GUI) is developed in the C++ environment. The information provided by the user will be read by MATLAB kernel, which is based on the algorithm proposed in Section 2 and 3. After the calculation is finished, results will be sent back to GUI and plotted there. The user can also export the calculation results in GUI.

4.2. GUI DESIGN

The GUI of single rack equivalent source reconstruction and multiple rack radiation prediction are designed separately. The dipole extraction part is shown in Figure 4.1. The left part are the input bars. The user needs to provide information such as radiation frequency, the position of two cylindrical scanning surfaces, and the electric field distribution on two surfaces. Once this information is provided, the distribution of observation points will be displayed at the lower left corner. After the source extraction is done, the field distribution on two scanning surfaces will be shown automatically. Users can select which E-field component they want to plot. The information of reconstructed dipoles is at the bottom right. Users can export this information into a csv file.

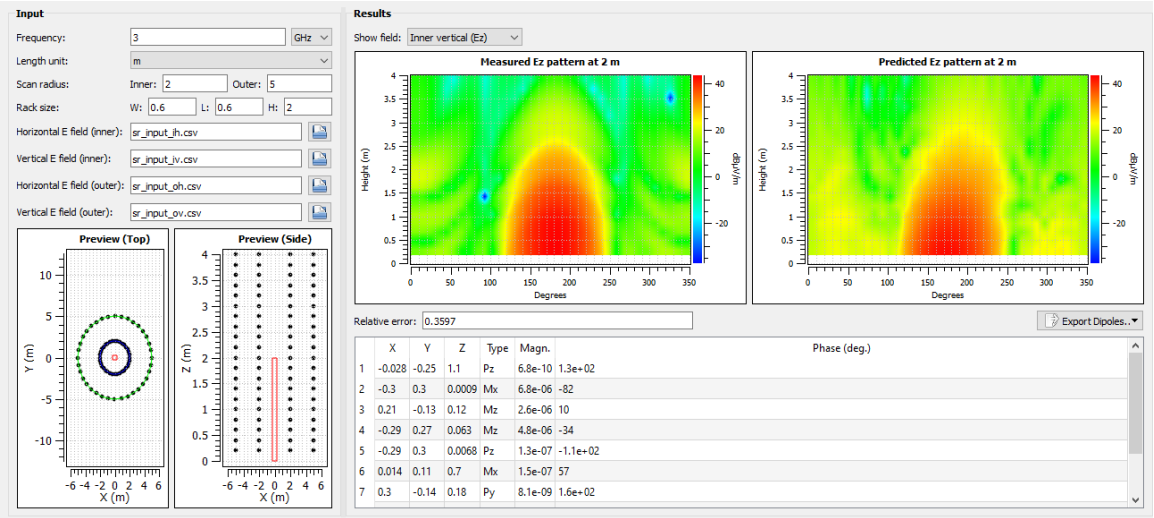

Figure 4.1. GUI design of single rack equivalent dipole source reconstruction

The GUI of multiple rack radiation calculation is more complicated. There are four tabs in the tool. The first tab is called 'General' as shown in Figure 4.2; the user needs to define the simulation frequency, the geometry information of data center building, and the wall attenuation information in this tab.

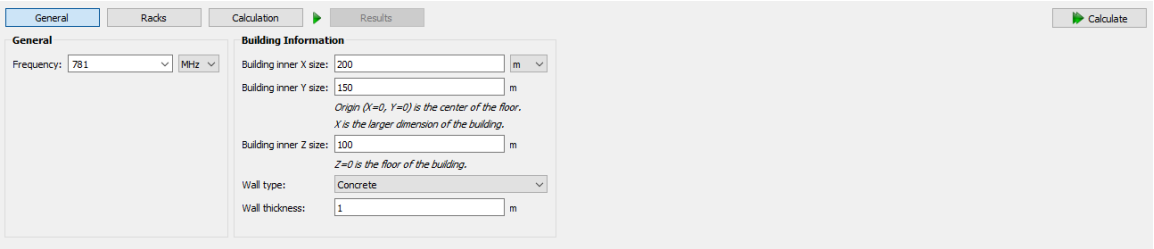

Figure 4.2. General tab of the multiple rack GUI

Next, in the 'Racks' tab shown in Figure 4.3, the user needs to type in the geometry information of the array, such as the number of rows and columns, the spacing between the racks, etc. In addition, the structure and equivalent dipole source of racks are also assigned by clicking the 'Library' button. Then a rack type library window will pop out as shown in

Figure 4.4. After receiving all this information, GUI will show a rack distribution preview on the right and a list of all racks at the bottom. The user can zoom in and out to check the rack positions at the distribution preview and turn some racks on or off in the rack list.

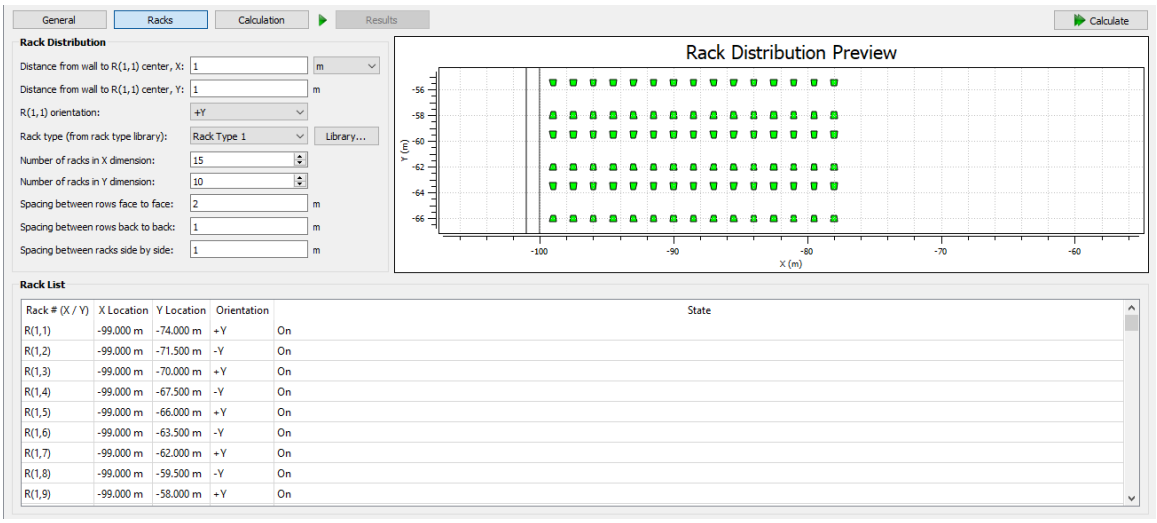

Figure 4.3. Racks tab of the multiple rack GUI

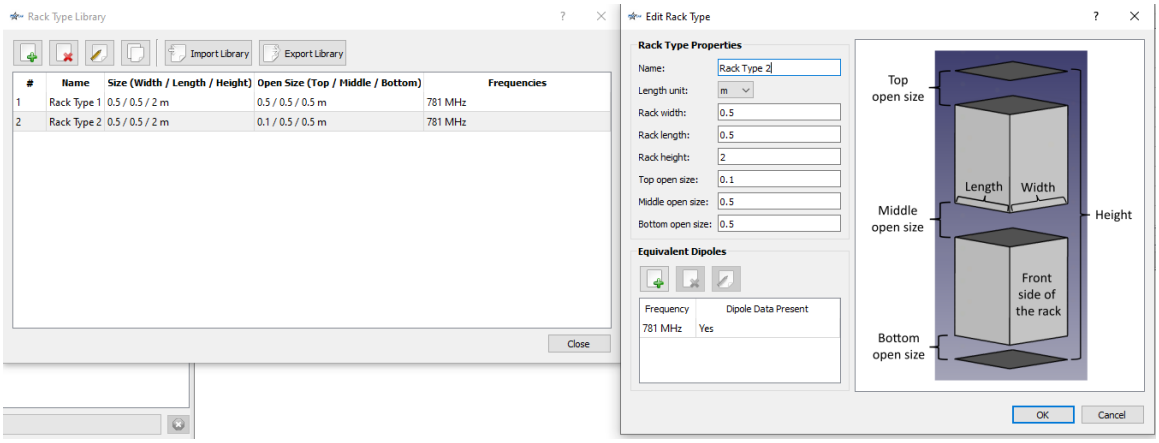

Figure 4.4. Rack library

Then, at the calculation tab, the user can define the observation surfaces. There are four types of observation surfaces available: cylindrical near field scan, spherical near field scan, single point near field scan, and spherical far field scan. The user can set the radius of the cylindrical and spherical scan, and the distance between two successive observation points and other parameters. There can be multiple scanning surfaces in one simulation.

After all the definitions in three tabs are complete, the user can click the calculation button on the top right to start the simulation.

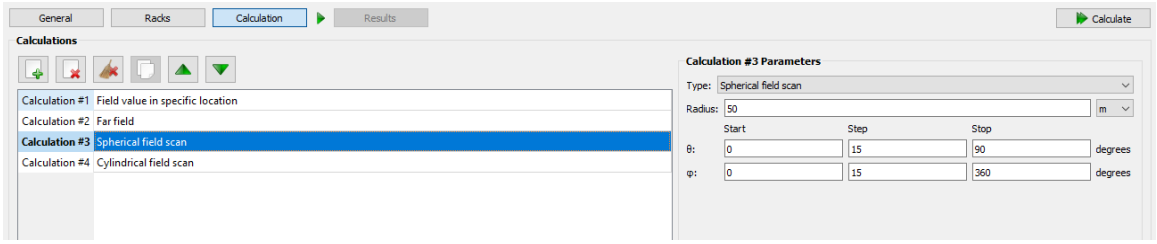

Figure 4.5. Calculation tab of the multiple rack GUI

After the simulation is completed, the result will be shown in the results tab, like the one in Figure 4.6. The user can select which filed component to plot and whether or not to include the attenuation of wall. The GUI will also show the maximum field value and the corresponding position.

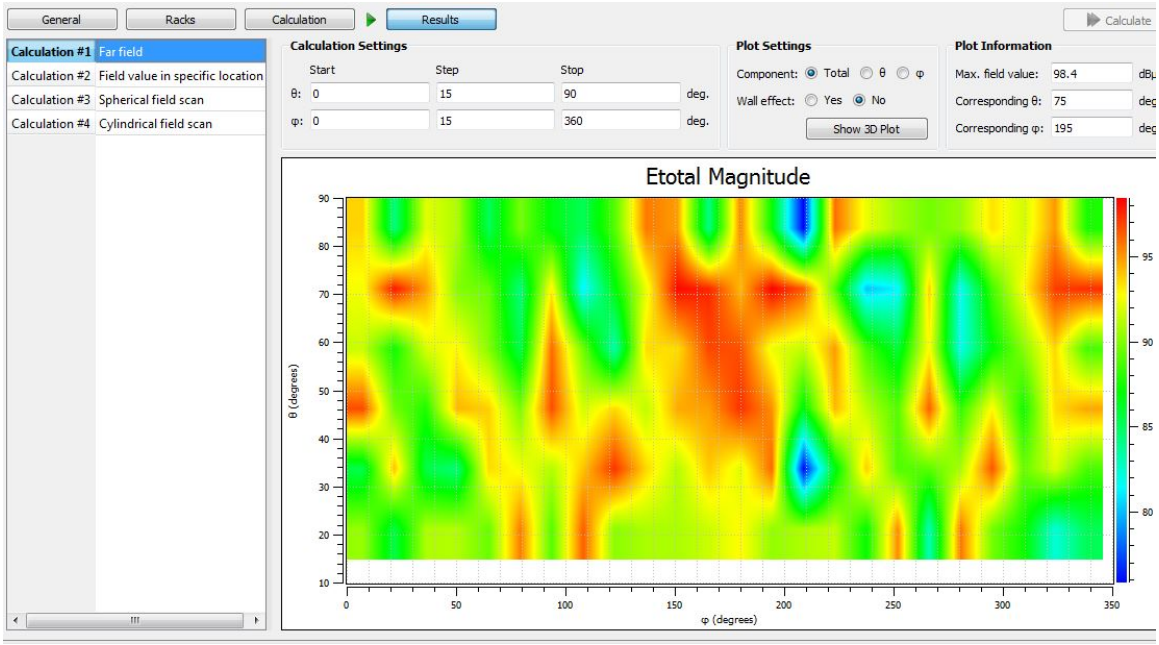

Figure 4.6. Results tab of the multiple rack GUI

4.3. KERNEL DEVELOPMENT

The algorithm of multiple rack radiation calculation kernel is discussed in Section 3. Her, the MATLAB coding issues in the kernel development will be discussed. The work flow of the kernel is shown in Figure 4.7.

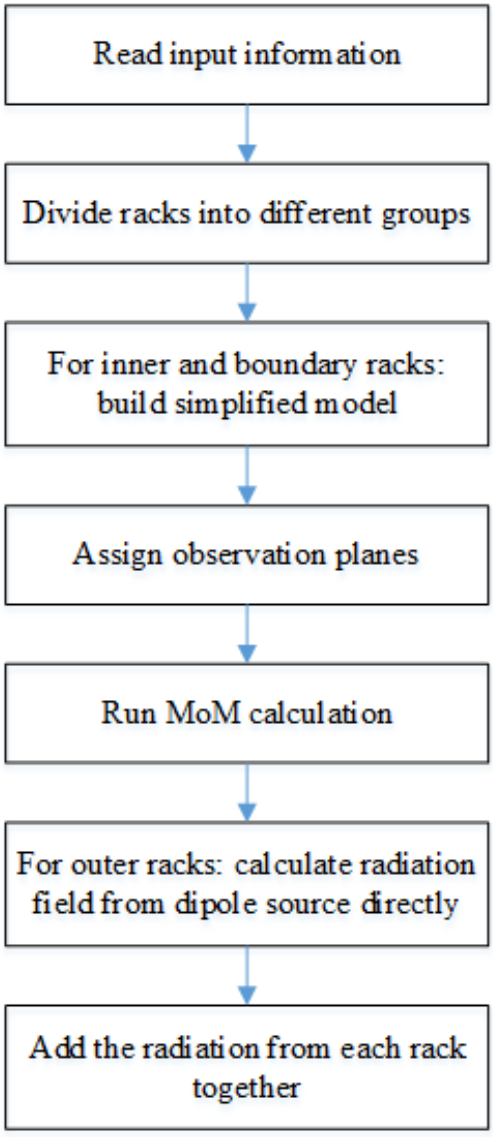

Figure 4.7. Code flow of multiple rack radiation calculation kernel.

The information provided by the user will be written into an .XML file, the first step of the kernel is to read this information. Next, racks will be divided into three groups: outer rack, inner rack, and boundary rack. The definition of the inner and boundary rack is determined by the simulation frequency. Then, the radiation of each inner and boundary rack will be calculated using the Method of Moments (MoM) solver. In order to do this, the simplified model discussed in section 3.3.2 is built automatically. The size of model is adjusted according to the user inputs. Then the model is discretized using triangular mesh by calling a third party tool, Gmsh [29]. One example of the meshed simplified model is shown in Figure 4.8. Next the kernel will assign the observation points. Since the simplified model of racks from the same group are the same, instead of running multiple simulations, the kernel will assign several different scanning surfaces in one model. In reality, the observation points are fixed while the radiation sources are located at different positions. Now there is only one fixed radiation source, the scanning surface need to be shifted in order to keep the relative position between the observation points and source unchanged.

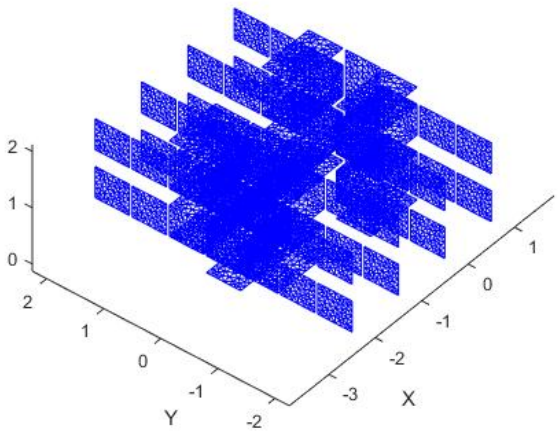

Figure 4.8. Simplified simulation model of inner rack at 781MHz.

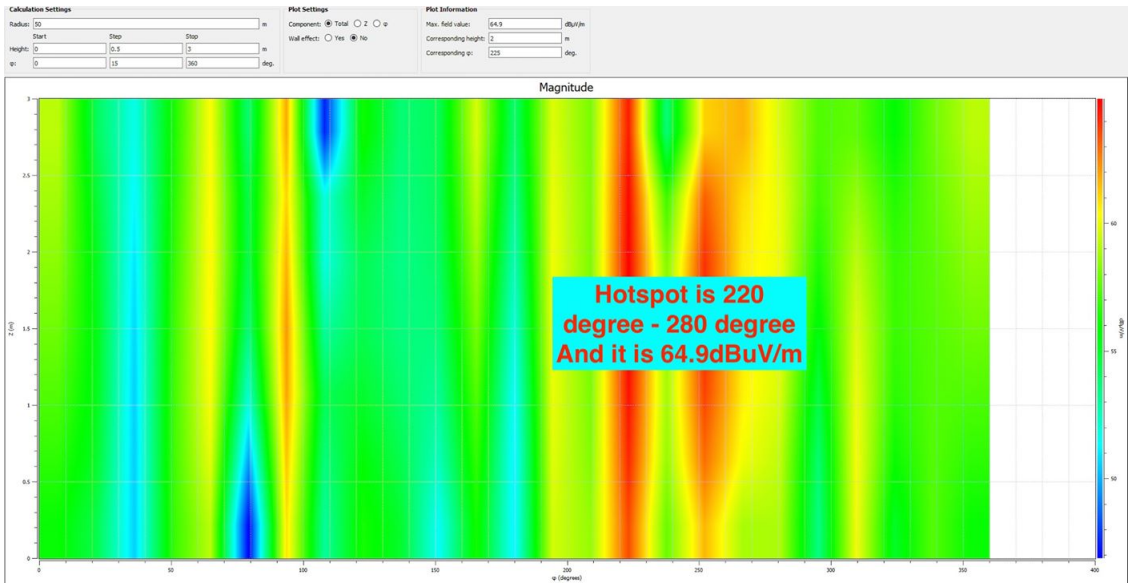

Figure 4.9. Simulated field distribution on cylindrical scanning surface.

For outer racks, things are much easier. Since all the rest of the rack structures can be neglected, we can use the equations in Section 2 to calculate the field distribution quickly.

After the radiation from each rack is calculated, they can be added together to get the final estimation result. The final data will be sent back to GUI and plotted there. Users can download these data for further investigation.

4.4. ALGORITHM VALIDATION

The proposed algorithm is validated by comparing the estimation result with measurement result. The emission field strength around one data center is measured. There are 1280 racks installed in the data center. Among them, 288 racks are radiating at 781 MHz. They are placed randomly inside the rack array. The highest emission is 66.7 $dB\mu V/m$ after factoring in cable loss, antenna factor, and pre-amplifier gain, and the azimuth of hotspot is from 260 degrees to 300 degrees.

In the simulation tool, the same rack array is built. There are 40 rows and 32 columns. Among them, 288 racks are randomly selected to be turned on, all the rest are turned off. These tuned off racks will not radiate at 781 MHz, but their metal structure will scatter the radiation field and further affect the field distribution, so they can not be ignored here.

After calculation, the estimated highest emission is 64.9 $dB\mu V/m$ and the hotspot azimuth is from 220 degrees to 280 degrees, both agrees with the measurement result. The simulation result is shown in Figure 4.9. The offset in azimuth could be caused by two factors. The source distribution in the simulation may not be exactly the same as the actual configuration. And there is a gap between the $16th$ column and $17th$ column in the real configuration, which is not included in the simulation model.

5. CONCLUSION

In this thesis, a method to estimate electromagnetic emissions from a site installation with multiple racks of server equipment is proposed, and a user friendly software tool is developed for future application. Simulating all the racks together is not feasible because of the limitation of time and computational resources. Instead, the total radiation of the data center is calculated by adding the contribution from each rack together. Racks in the array can be divided into several categories according to their position. Racks in the same category have similar radiation field distribution. Thus for each category, the emission from one represent rack is calculated using MoM. In the simulation model, the radiating rack is replaced by the equivalent dipole moment which is extracted from a single rack near field scanning result. The coupling between racks can affect the final field distribution significantly, and it is found that the effect of nearby racks is important while the rest racks can be neglected. Based on this discovery, the simulation model is simplified and validated by simulation and measurement. Radiation of the rest racks can be obtained by shifting, rotating or flipping the field of the corresponding representative rack. Finally, the total radiation of the data center is obtained by vector summing the individual contributions of all the racks in the data center. This method is much faster than the brute-force simulation of the entire data center, and is highly scalable to handle an arbitrary number of racks in the data center.

REFERENCES

[1] L. Zhang, X. Li, X. Jiao, J. Li, S. S. Toor, A. U. Bhobe, D. J. Pommerenke, and J. L. Drewniak, "Emi coupling paths and mitigation in optical transceiver modules," *IEEE Transactions on Electromagnetic Compatibility*, vol. 59, no. 6, pp. 1848–1855, 2017.

[2] J. Li, X. Li, X. Jiao, S. Toor, L. Zhang, A. Bhobe, J. Drewniak, and D. Pommerenke, "Emi coupling paths in silicon optical sub-assembly package," in *2016 IEEE International symposium on electromagnetic compatibility (EMC)*, pp. 890–895, 2016.

[3] P. Shen, Y. Qi, W. Yu, F. Li, and J. Fan, "Fast method for ota performance testing of transmit-receive cofrequency mobile terminal," *IEEE Transactions on Electromagnetic Compatibility*, vol. 58, pp. 1367–1374, 2016.

[4] S. Yong, S. Yang, L. Zhang, X. Chen, D. J. Pommerenke, and V. Khilkevich, "Passive intermodulation source localization based on emission source microscopy," *IEEE Transactions on Electromagnetic Compatibility*, 2019.

[5] L. Zhang, V. V. Khilkevich, X. Jiao, X. Li, S. Toor, A. U. Bhobe, K. Koo, D. Pommerenke, and J. L. Drewniak, "Sparse emission source microscopy for rapid emission source imaging," *IEEE Transactions on Electromagnetic Compatibility*, vol. 59, no. 2, pp. 729–738, 2017.

[6] M. Sørensen, H. Kajbaf, V. V. Khilkevich, L. Zhang, and D. Pommerenke, "Analysis of the effect on image quality of different scanning point selection methods in sparse esm," *IEEE Transactions on Electromagnetic Compatibility*, 2018.

[7] Y. S. Cao, X. Wang, W. Mai, Y. Wang, L. Jiang, A. E. Ruehli, S. He, H. Zhao, J. Hu, J. Fan, *et al.*, "Characterizing emi radiation physics for edge-and broad-side coupled connectors," pp. 766–771, 2017.

[8] Y. S. Cao, Y. Wang, L. Jiang, A. E. Ruehli, J. Fan, and J. L. Drewniak, "Quantifying emi: a methodology for determining and quantifying radiation for practical design guidelines," *IEEE Transactions on Electromagnetic Compatibility*, vol. 59, no. 5, pp. 1424–1432, 2017.

[9] Q. Huang, L. Li, X. Yan, B. Bae, H. Park, C. Hwang, and J. Fan, "Mom based current reconstruction using near-field scanning," in *2017 IEEE International Symposium on Electromagnetic Compatibility & Signal/Power Integrity (EMCSI)*, pp. 549–554, 2017.

[10] Q. Huang, F. Zhang, T. Enomoto, J. Maeshima, K. Araki, and C. Hwang, "Physics-based dipole moment source reconstruction for rfi on a practical cellphone," *IEEE Transactions on Electromagnetic Compatibility*, vol. 59, no. 6, pp. 1693–1700, 2017.

[11] C. Hwang and Q. Huang, "Ic placement optimization for rf interference based on dipole moment sources and reciprocity," in *2017 Asia-Pacific International Symposium on Electromagnetic Compatibility (APEMC)*, pp. 331–333, 2017.

[12] Q. Huang and J. Fan, "Machine learning based source reconstruction for rf desense," *IEEE Transactions on Electromagnetic Compatibility*, vol. 60, no. 6, pp. 1640–1647, 2018.

[13] Z. Yu, J. A. Mix, S. Sajuyigbe, K. P. Slattery, and J. Fan, "An improved dipole-moment model based on near-field scanning for characterizing near-field coupling and far-field radiation from an ic," *IEEE Transactions on electromagnetic compatibility*, vol. 55, no. 1, pp. 97–108, 2012.

[14] Q. Huang, Y. Zhong, C. Hwang, J. Fan, J. Rajagopalan, D. Pai, C. Chen, and A. Gaikwad, "Desense prediction and mitigation from ddr noise source," in *2018 IEEE Symposium on Electromagnetic Compatibility, Signal Integrity and Power Integrity (EMC, SI & PI)*, pp. 139–144, 2018.

[15] Q. Huang, L. Li, X. Yan, B. Bae, H. Park, C. Hwang, and J. Fan, "Mom-based ground current reconstruction in rfi application," *IEEE Transactions on Electromagnetic Compatibility*, vol. 60, no. 4, pp. 1121–1128, 2018.

[16] Q. Huang, Y. Liu, L. Li, Y. Wang, C. Wu, and J. Fan, "Radio frequency interference estimation using transfer function based dipole moment model," in *2018 IEEE International Symposium on Electromagnetic Compatibility and 2018 IEEE Asia-Pacific Symposium on Electromagnetic Compatibility (EMC/APEMC)*, pp. 115–120, 2018.

[17] Q. Huang, D. Pai, K. Rao, A. Mohan, J. Vutukury, C.-M. Nieh, J. Fan, and J. Rajagopalan, "Accurate prediction and mitigation of emi from high-speed noise sources using full wave solver," in *2019 IEEE International Symposium on Electromagnetic Compatibility, Signal & Power Integrity (EMC+ SIPI)*, pp. 595–599, 2019.

[18] Q. Huang, J. Li, J. Zhou, W. Wu, Y. Qi, and J. Fan, "De-embedding method to accurately measure high-frequency impedance of an o-shape spring contact," in *2014 IEEE International Symposium on Electromagnetic Compatibility (EMC)*, pp. 600–603, 2014.

[19] Y. Zhong, Q. Huang, T. Enomoto, S. Seto, K. Araki, and C. Hwang, "Measurement-based characterization of buzz noise in wireless devices," in *2018 IEEE Symposium on Electromagnetic Compatibility, Signal Integrity and Power Integrity (EMC, SI & PI)*, pp. 134–138, 2018.

[20] Q. Huang, T. Enomoto, S. Seto, K. Araki, J. Fan, and C. Hwang, "A transfer function based calculation method for radio frequency interference," *IEEE Transactions on Electromagnetic Compatibility*, 2019.

[21] J. Zhang and J. Fan, "Source reconstruction for ic radiated emissions based on magnitude-only near-field scanning," *IEEE Transactions on Electromagnetic Compatibility*, vol. 59, no. 2, pp. 557–566, 2017.

[22] J.-M. Jin, *Theory and computation of electromagnetic fields*. John Wiley & Sons, 2011.

[23] T. S. Sijher and A. A. Kishk, "Antenna modeling by infinitesimal dipoles using genetic algorithms," *Progress In Electromagnetics Research*, vol. 52, pp. 225–254, 2005.

[24] Y. Wang, Y. S. Cao, J. Fan, S. Wu, Z. Yang, S. Jin, J. Zhang, and T. Li, "Correcting antenna pattern in offset measurements based on equivalent dipole moments," in *2018 IEEE Symposium on Electromagnetic Compatibility, Signal Integrity and Power Integrity (EMC, SI & PI)*, pp. 493–498, 2018.

[25] C. Wu, Z. Sun, Q. Huang, Y. Wang, J. Fan, and J. Zhou, "A method to extract physical dipoles for radiating source characterization and near field coupling estimation," in *2019 IEEE International Symposium on Electromagnetic Compatibility, Signal & Power Integrity (EMC+ SIPI)*, pp. 580–583, 2019.

[26] C. A. Balanis, *Antenna theory: analysis and design*. John wiley & sons, 2016.

[27] T. M. Inc, *What Is the Genetic Algorithm?*, accessed October 16, 2019.

[28] A. E. Inc, *Altair Feko™ Overview*, accessed October 16, 2019.

[29] C. Geuzaine and J.-F. Remacle, *Gmsh: A three-dimensional finite element mesh generator with built-in pre- and post-processing facilities*, accessed October 16, 2019.

VITA

Ze Sun received his Bachelor of Engineering degree in Optoelectronic Information Science and Engineering from Huazhong University of Science and Technology, China in June 2017. He worked on Electromagnetic Interference in the EMC laboratory from 2017 to 2019. He received the Master of Science degree in Electrical Engineering from Missouri University of Science and Technology, USA in December 2019.